Noise-Aware Entanglement Generation Protocols for Superconducting Qubits with impedance-matched FBAR Transducers

Erin Sheridan,[1] Michael Senatore,[1] Samuel Schwab,[1] Eric Aspling,[2] Taylor Wagner,[3] James Schneeloch,[1] Stephen McCoy,[4] Daniel Campbell,[1] David Hucul,[1] Zachary Smith,[1] and Matthew LaHaye[1]

[1] *U.S. Air Force Research Laboratory, Information Directorate, Rome, NY 13441*
[2] *Griffiss Institute, Rome, NY 13441*
[3] *Technergetics, Rome, NY 13441*
[4] *Booz Allen Hamilton, Rome, NY 13441*
(Dated: April 11, 2025)

Connecting superconducting quantum processors to telecommunications-wavelength quantum networks is critically necessary to enable distributed quantum computing, secure communications, and other applications. Optically-mediated entanglement heralding protocols offer a near-term solution that can succeed with imperfect components, including sub-unity efficiency microwave-optical quantum transducers. The viability and performance of these protocols relies heavily on the properties of the transducers used: the conversion efficiency, resonator lifetimes, and added noise in the transducer directly influence the achievable entanglement generation rate and fidelity of an entanglement generation protocol. Here, we use an extended Butterworth-van Dyke (BVD) model to optimize the conversion efficiency and added noise of a Thin Film Bulk Acoustic Resonator (FBAR) piezo-optomechanical transducer. We use the outputs from this model to calculate the fidelity of one-photon and two-photon entanglement heralding protocols in a variety of operating regimes. For transducers with matching circuits designed to either minimize the added noise or maximize conversion efficiency, we theoretically estimate that entanglement generation rates of greater than 160 kHz can be achieved at moderate pump powers with fidelities of $> 90\%$. This is the first time a BVD equivalent circuit model is used to both optimize the performance of an FBAR transducer and to directly inform the design and implementation of an entanglement generation protocol. These results can be applied in the near term to realize quantum networks of superconducting qubits with realistic experimental parameters.

I. INTRODUCTION

Microwave-optical quantum transducers [1–3] are critical components for connecting superconducting qubits to quantum networks [4–6], toward distributed quantum computing [7], secure communications [8], and other applications requiring entanglement distribution between heterogeneous network nodes. These devices are tasked with coherently converting quantum information between frequencies separated by five orders of magnitude, from $\sim$ 5 GHz to $\sim$ 193 THz. In contrast to deterministic entanglement distribution protocols, optically heralded schemes [9, 10] can operate effectively with low-efficiency transducers [11, 12]. While heralded entanglement demonstrations have been carried out with atom-based qubits [13–17] and optically active solid-state qubits [18–20], where flying optical photons entangled to each remote node mediate the generation of entanglement between them, the same cannot be said for superconducting qubits. In recent years, microwave-optical transducers have improved enough, in principle, to allow initial demonstrations of heralded photon entanglement between superconducting quantum systems via a telecom fiber link. Though entanglement between remote superconducting qubits has been established using microwave interconnects [21–23], there has been no experimental demonstration of optically-mediated entanglement generation between remote superconducting quantum circuits to date. This may be because previous efforts to integrate superconducting qubits with microwave-optical transducers have been limited by prohibitively low qubit coherence times and high added noise due to heat dissipation in the transducer [24, 25], as well as limited cooling power in cryogenic systems.

Piezo-optomechanical transducers are reaching a point in their maturity where experimental demonstrations of heralded entanglement protocols [6, 28–31] are possible. As shown in Figure 1(a), these transducers achieve coherent microwave-optical conversion by first converting a microwave photon to an acoustic phonon via the piezoelectric effect, with electromechanical coupling rate g_{EM}, then converting the phonon to an optical photon via radiation pressure or the stress-optical effect, with a cavity-enhanced optomechanical coupling rate g_{OM}. In the next section, we will introduce a specific class of piezo-optomechanical transducers. We will then proceed to design impedance-matching circuits for these devices, then explore their operation within entanglement heralding protocols.

A. The FBAR Piezo-optomechanical transducer

Transducers based on optomechanical crystal (OMC) cavities have achieved high conversion efficiencies[25, 32, 33]. However, these devices suffer from high added noise quanta per transduced photon, as the OMC cavity is susceptible to optical absorption-based heating [34], leading

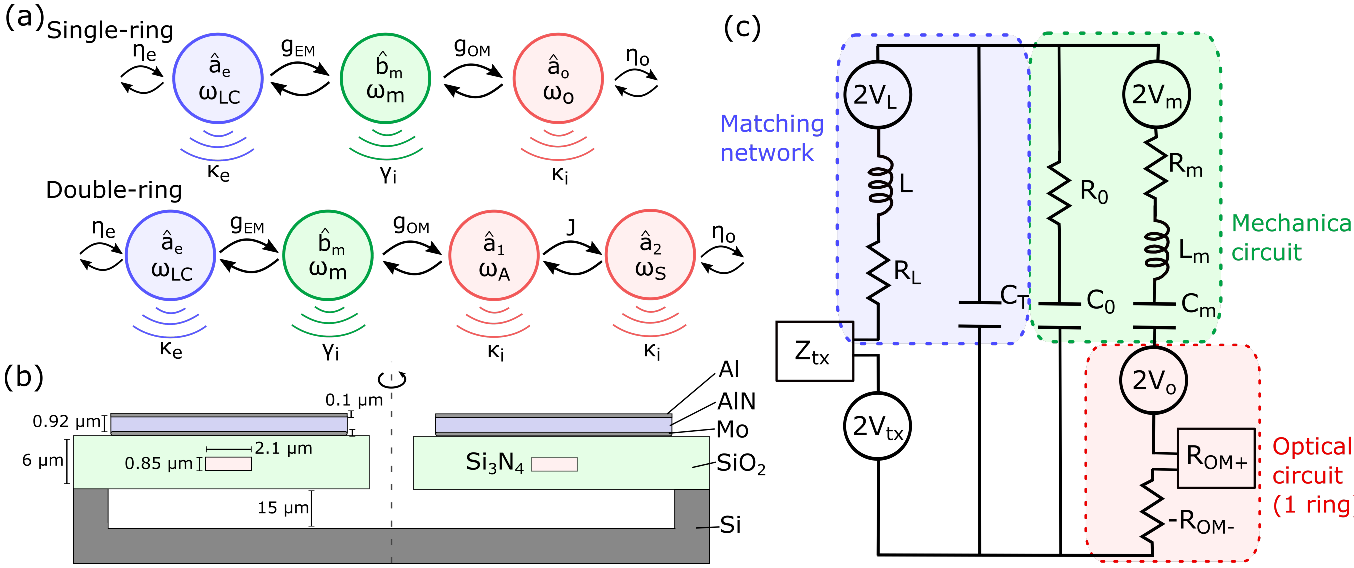

FIG. 1. (a) Schematic of the constituent modes of a piezo-optomechanical transducer and their interactions with each other and the outside world for (top) a single-ring device and (bottom) a double-ring device. g_{EM} is the electromechanical coupling rate, g_{OM} is the optomechanical coupling rate, η_e is the microwave signal coupling efficiency, κ_e is the microwave mode ($\hat{a}_e$) loss J is the optical-optical coupling rate, rate, γ_i is the mechanical mode ($\hat{b}_m$) intrinsic linewidth, κ_i is the optical mode ($\hat{a}_o$, $\hat{a}_A$, $\hat{a}_S$) intrinsic linewidth, and η_o is the optical mode external coupling efficiency. (b) Side profile of an example material stack for an FBAR transducer, adapted from [26]. The dashed line denotes the axis of rotational symmetry. General estimates of layer thicknesses are shown, and should be understood as rough guides. Specific FBAR devices may have slightly modified dimensions. (c) Thévenin equivalent circuit for a piezo-optomechanical transducer, including a matching network. Z_{tx} is the input impedance, L is the matching inductor, C_T is the matching capacitor, R_L is the matching inductor's resistance, C_0 is the static capacitance, R_0 is the static resistance, R_m, L_m, C_m are the motional resistance, inductance, and capacitance, respectively, $R_{OM\pm}$ are the equivalent resistances for the optical signal and noise outputs, and V_{tx}, V_L, V_m, V_o are the Thévenin equivalent voltage sources which accompany every resistive element. for the Adapted from [27].

to non-negligible thermal Brownian motion of the mechanical modes [24]. Recently, two-dimensional OMCs have been developed to enhance thermalization [35, 36] and have achieved thermal occupancies of the phonon cavity < 1 at high optical pump repetition rates with optical cavity occupations on the order of 10^3 photons. These results motivate the exploration of bulk acoustic resonators for even better thermalization, promising acoustic cavity ground state operation at even higher optical cavity occupations.

As an alternative to transducers based on OMCs, transducers utilizing bulk acoustic resonators, such as the Thin Film Bulk Acoustic Resonator (FBAR) devices [26, 37–39] promise superior power handling capabilities [40–42] and high electromechanical extraction and phonon injection efficiencies [43], in addition to the advantage of their compatibility with CMOS foundry fabrication. The bulk nature of these devices may allow for higher pump powers and repetition rates while maintaining fewer added noise quanta per transduced photon, since heat can propagate through the bulk of the chip. Bulk acoustic modes have been integrated with superconducting circuits in the past and have achieved strong coherent coupling [44, 45]. Furthermore, the degeneracy of the microwave and mechanical modes in FBAR devices eliminates the need to tune the microwave and mechanical modes into resonance, using magnetic fields from e.g. microwave coils installed within a dilution refrigerator [33], significantly reducing the complexity of operation.

In this work, we design impedance-matching networks and entanglement heralding protocols for the FBAR transducer, following the work done by Wu *et al.* [27] on matching network design and by Zeuthen *et al.* [28] on heralding protocol design. A side profile of an FBAR transducer is shown in Figure 1(b). These converters utilize high-overtone bulk acoustic resonances (HBARs) as an intermediary between microwave and optical modes. For microwave-to-optical conversion, microwave signals encounter a microwave cavity consisting of an aluminum nitride (AlN) piezoelectric film sandwiched between signal and ground electrodes. During the electromechanical interaction, these electrical signals generate expansion and contraction of the film through the converse piezoelectric effect; these expansions and contractions in turn launch acoustic waves into the transducer's acoustic cavity. When the cavity length is equal to an integer multiple of the acoustic wavelength, multiple acoustic standing waves interfere constructively, leading to a resonant feature (an HBAR mode). The optomechanical interaction arises from the acoustic resonances modifying the index of refraction of an optical micro-ring resonator (MRR) via the stress-optical effect.

Intermediate-mode transducers, including piezo-optomechanical devices, can be described by the generic interaction Hamiltonian

$$H_{int} = \hbar \sum_{i=e,o} g_{iM}(\hat{b}_m e^{-i\omega_m t} + \hat{b}_m^\dagger e^{i\omega_m t})(\hat{a}_i e^{-i\Delta_i t} + \hat{a}_i^\dagger e^{i\Delta_i t}) \tag{1}$$

for the mechanical mode $\hat{b}_m$ with angular frequency ω_m, coupling rates g_{iM} and a pump-cavity detuning defined as $\Delta_i = \omega_i - \omega_{pump}$ for modes $\hat{a}_i$. In FBAR transducers the mechanical mode and microwave mode are degenerate, so the mechanical field can be taken as pumped directly by the microwave field with an input-output relation of $\hat{a}_{e,in} + \hat{a}_{e,out} = \sqrt{\gamma_{ex}}\hat{b}_m$ [26, 39] for a microwave photon-phonon coupling rate $\gamma_{ex} \sim {}^{4g_{EM}^2}/_{\Gamma}$ with microwave cavity linewidth Γ. This simplifies the interaction Hamiltonian, which can now be written as

$$H_{int} = \hbar g_{OM}(\hat{b}_m e^{-i\omega_m t} + \hat{b}_m^\dagger e^{i\omega_m t})(\hat{a}_o e^{-i\Delta_o t} + \hat{a}_o^\dagger e^{i\Delta_o t}) \tag{2}$$

with pump-optical mode detuning Δ_o. We can select one of two possible optomechanical interactions by red-detuning our pump laser pulse such that $\Delta_o = \omega_m$ or blue-detuning the pulse such that $\Delta_o = -\omega_m$ [2]. Multiplying out the optomechanical interaction terms and discarding high-frequency terms oscillating at $\pm 2\omega_m$, we have, for the red-detuned case,

$$H_{int,red} = \hbar g_{OM}(\hat{b}_m^\dagger \hat{a}_o + \hat{b}_m \hat{a}_o^\dagger) \tag{3}$$

yielding a beamsplitter-like interaction between the optical cavity mode and the mechanical mode, where excitations are swapped between modes. The red-detuned optical pump, together with a resonant microwave pump, enables direct microwave-to-optical transduction. A blue-detuned pump $\Delta_o = \omega_m$ leads to optomechanical two-mode squeezing interaction:

$$H_{int,blue} = \hbar g_{OM}(\hat{b}_m \hat{a}_o + \hat{b}_m^\dagger \hat{a}_o^\dagger) \tag{4}$$

which will not be the focus of this work. Finally, if we incorporate a second optical mode, we re-label the modes as $\hat{a}_1$ and $\hat{a}_2$ coupled with rate J. We can write the complete red-detuned interaction Hamiltonian as [26]

$$H_{int,red} = \hbar g_{OM}(\hat{b}_m^\dagger \hat{a}_1 + \hat{b}_m \hat{a}_1^\dagger) + \hbar J(\hat{a}_1^\dagger \hat{a}_2 + \hat{a}_1 \hat{a}_2^\dagger). \tag{5}$$

More details on the theoretical foundations underpinning FBAR transducer operation can be found in references [26, 37–39].

B. Butterworth-van Dyke model and impedance matching

A disadvantage of FBAR transducers is their comparatively low optomechanical coupling rates [43]. An estimate based on finite-element simulations for a layout similar to that shown in Figure 1(b) puts the single-photon optomechanical coupling rate at 400 Hz [26]. This low coupling rate limits the conversion efficiency of the device for low optical pump powers. In Blesin *et al.*[26], a peak on-chip microwave-optical conversion efficiency of 40% was theoretically estimated for an optical pump power of 100 mW. While promising, achieving such high pump powers on chip is unrealistic in a milli-Kelvin cryogenic environment, and would likely introduce large amounts of thermal noise in the transducer that would preclude the ability to coherently transduce quantum information.

The performance of the FBAR devices can be improved by the use of electrical impedance-matching networks, which are used to boost signal transfer efficiency [27, 46]. Impedance matching networks can be used to either maximize the conversion efficiency of the transducer by balancing its cooperativities, or minimize added noise by maximizing the electromechanical coupling rate. To design such networks, we first need to formulate an equivalent circuit representation of the transducer.

The BVD model is an equivalent circuit model that has been used extensively to understand the behavior of FBAR acoustic devices [8, 27, 37, 43, 47]. Impedance matching networks can be designed within an expanded BVD equivalent circuit model that captures the behavior of the entire transducer [27, 46]. What's more, the physical parameters needed as inputs for the extended BVD model, including the transducer's static capacitance and its electromechanical coupling factor ($k_{eff}^2 = {}^{4g_{EM}{}^2}/_{\omega_m^2}$ for resonant microwave and mechanical modes), can be extracted in a straightforward way from finite-element simulations [47]. In Sec. II we use the extended BVD model to design impedance matching networks for FBAR transducers with a single optical cavity and with two coupled optical cavities.

Here, for the first time, we show that the BVD model can be used not only to optimize an optomechanical transducer, but also to optimize optically-mediated entanglement heralding protocols making use of these transducers.

C. Entanglement heralding for superconducting qubits

Often referred to as the DCLZ [9] or Barrett-Kok [10] protocol, optically-mediated entanglement of remote

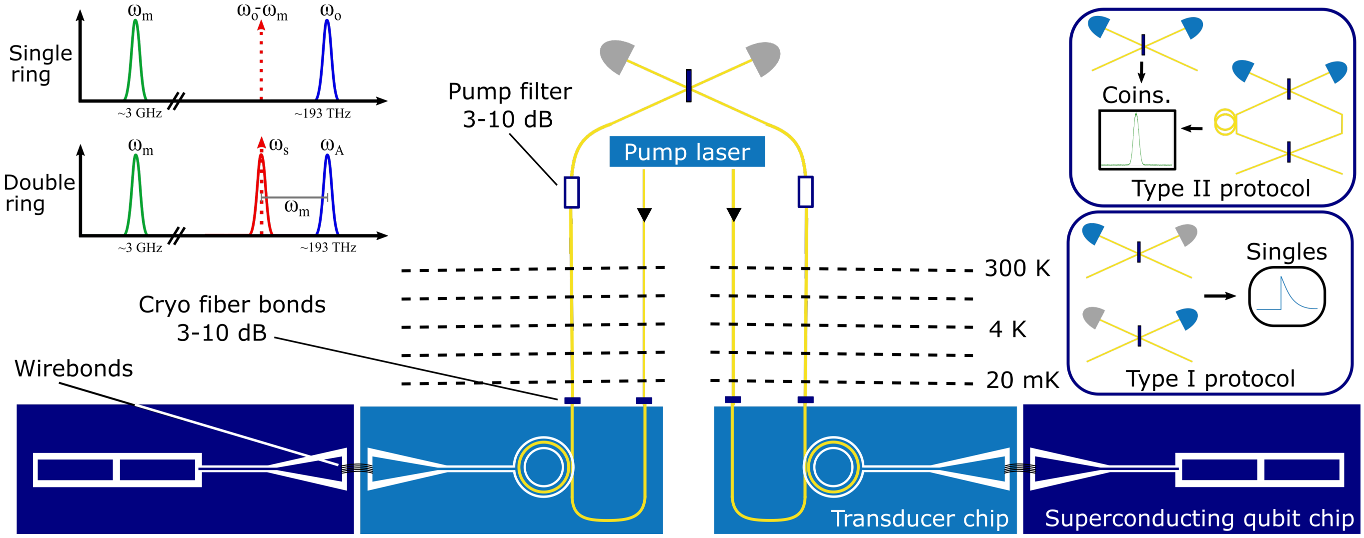

FIG. 2. Diagram of an entanglement heralding setup between two nominally identical quantum network nodes consisting of generic superconducting circuits and microwave-optical transducers, which are located within cryostats operating at 20 mK base temperature. A single-ring transducer is depicted. A laser sends red-detuned pump pulses to the transducers. Top left shows simplified density of states diagrams for red-detuned pumping of single-ring and double-ring FBAR transducers. Microwave electronics send drive pulses to the superconducting qubits via coaxial cables (not shown) to initialize them in the excited state. Photons output from each transducer coupled off-chip via cryogenic fiber bonds, with a typical loss of $3-10$ dB, then undergo pump filtering, also with a typical loss of $3-10$ dB, before impinging on a Bell state analyzer (BSA) with a 50:50 beamsplitter. For the Type I protocol, single photon detection events in either photodetector herald entanglement between the remote superconducting qubits. For the Type II protocol, coincident detection events (coins) do the same, using either a balanced or unbalanced BSA.

matter-based qubits involves interfering flying photons emitted by those qubits in a Bell state analyzer. The beamsplitter within the analyzer erases which-path information before the photon(s) are incident upon single photon detectors. This information erasure allows one to project entanglement onto the remote quantum memories. These protocols can broadly be classified as one-photon (Type I) or two-photon (Type II) protocols [48].

A Type-I protocol is that which uses an optical single-photon state to establish a distributed Bell state between matter-based qubits at remote network nodes. It will only succeed when one photon is emitted, in total, from both network nodes. As detailed below, Type-I protocols are susceptible to sources of infidelity from two-photon emission events. They are also sensitive to path-length variations within the experimental setup, where even slight changes in the length of the network links can change the relative phase of the entangled state, leading to decoherence.

The phase stability requirement for Type-I protocols [19, 49] incentivizes the development of Type-II protocols, which are more robust to instabilities due to path-length variations. They are also immune to some sources of infidelity that affect Type-I protocols. The cost of these improvements is increased experimental complexity: quantum information is no longer encoded in a number state, but must be encoded in the time-bin, polarization, frequency, or other degrees of freedom of the optical photons[48].

When we consider heralding protocols in the context of superconducting qubits and transducers, even more complexities are introduced. As discussed above, the transducer can operate in different regimes depending on the frequency of the optical pump with respect to the optical cavity mode(s). Spontaneous parametric down-conversion (SPDC) operation is induced by an optical pump blue-detuned from the optical cavity (Equation 4),2 whereas a red-detuned optical pump yields a beam-splitter-type interaction that can be utilized for quantum coherent state transfer (direct transduction, Equation 3) [50]. SPDC operation generates entangled microwave-optical photon pairs within the transducer, where the microwave photon can then be swapped into a superconducting qubit. Zhong *et al.*[29] proposed a Type-II heralding protocol utilizing blue-detuned pumping for SPDC operation of the transducer and time-bin encoded optical photons. Recently, non-classically correlated microwave-telecom photon pair generation has been experimentally demonstrated [32, 51].

In contrast to SPDC operation, direct operation requires the transducer to capture a microwave photon emitted by a qubit. Direct operation allows us to avoid populating the transducer's acoustic mode with multi-phonon states, which is a significant source of infidelity. In this work we focus on red-detuned transducer operation, as it is experimentally more straightforward to implement and has been shown to generate higher fidelity entanglement generation[12] than SPDC-based heralding protocols for superconducting qubits.

Zeuthen *et al.* [28] previously explored the dependence of entanglement fidelity on the conversion efficiency and added noise associated with a microwave-optical quantum transducer [28]. Here we build off of that work, using outputs from the extended BVD model to obtain estimates for the fidelity of these protocols for an FBAR transducer in the presence of thermal noise. As a result, for the first time, we show how the BVD model can be used to optimize the transducer's figures of merit and those of a heralding protocol. Insights gleaned from our simulations can be used to precisely engineer transducers for optimal operation within a specific environment and protocol.

II. IMPEDANCE MATCHING NETWORKS FOR FBAR TRANSDUCERS

Impedance matching is a well-known technique for maximizing power transfer, minimizing signal reflections, or enhancing signal-to-noise in a network of elements with varying impedance. In the domain of radio frequency and microwave quantum circuitry, this technique has been utilized for an array of applications involving ultra-sensitive measurement of solid-state quantum electronic and electromechanical devices [52, 53]. A common approach in these applications is to utilize impedance matching L-networks, which consist of lumped element inductors and capacitors to cancel the reactive (imaginary) part of the load impedance, while transforming the real part to match the source impedance [54]. Such networks can be used to maximize signal transfer in an optomechanical transducer by forming a bridge between a 50 Ohm input impedance and a higher-impedance piezoelectric element.

When we apply this idea to optomechanical transducers, we need to think somewhat differently about the quantities we need to match. Specifically, we want the matching network to match the electromechanical loading and the optomechanical loading on the acoustic mode. At the same time, the resonant frequency of the matching circuit must match that of the acoustic mode [27]. To determine the parameters necessary to achieve these conditions simultaneously, we utilize an equivalent circuit representation constructed from the BVD model, as described below.

A. The BVD model

A BVD equivalent circuit for a piezo-mechanical element consists of both a static arm and a motional arm. Within the static arm, the static capacitor C_0 captures the usual capacitive behavior of the device's electrodes. The mechanical motion is described by the motional arm, the motional inductance L_m and motional capacitance C_m capture the mechanical kinetic and potential energy,

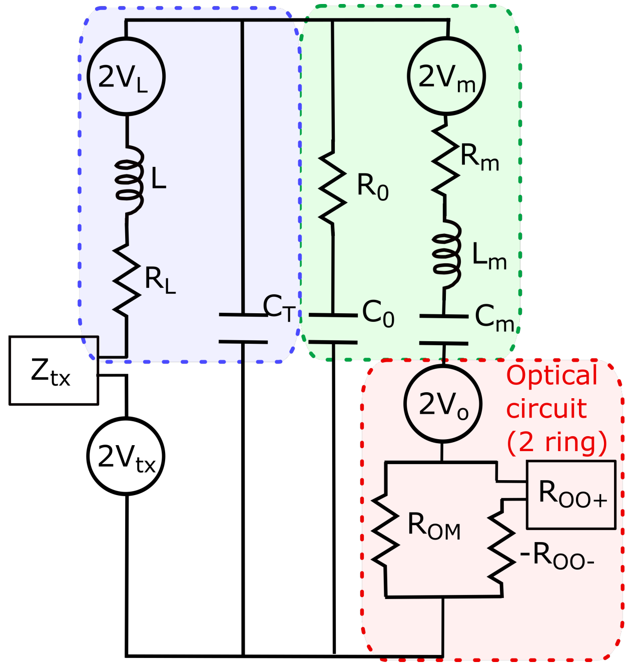

FIG. 3. A modified equivalent circuit for a transducer with two optical ring resonators. The three sub-circuits are the matching network (blue), mechanical sub-circuit (green) and the optical sub-circuit (orange). As compared to the equivalent circuit shown in Figure 1(c), the optical sub-circuit has been changed here. The optomechanical coupling is now represented by the effective resistance R_{OM} and the effective resistors $R_{OO\pm}$, representing the upper and lower optical sidebands, have been added in parallel with R_{OM}.

respectively, and a motional resistance R_m represents the dissipation of acoustic waves.

Generally, within the BVD model, one defines the electromechanical coupling factor as [55].

$$k_{eff}^2 = C_m/(C_0 + C_m) \tag{6}$$

However, as we will show in Sec. II B 1, for FBAR transducers $C_m \ll C_0$ and as such, we define the motional elements in the familiar form:

$$C_m = k_{eff}^2 C_0 \tag{7}$$

$$L_m = \frac{1}{\omega_m^2 C_m} \tag{8}$$

$$R_m = \gamma_m L_m \tag{9}$$

with acoustic mode ω_m that exhibits an intrinsic linewidth γ_m.

The behavior of a piezo-mechanical device is understood by examining its admittance

$$Y(\omega) = i\omega C_0 + \frac{1}{L_m}\frac{i\omega}{-\omega^2 + i\omega\gamma_m + \omega_m^2}. \tag{10}$$

Near resonance with a mechanical mode at ω_m, the imaginary part of the admittance curve will exhibit both a peak and a dip. The peak appears at the series resonant frequency ω_s and the dip appears at the parallel resonant frequency ω_p. The electromechanical coupling factor k_{eff}^2 can be defined with respect to the series-parallel frequency separation:

$$k_{eff}^2 = \frac{\omega_p^2 - \omega_s^2}{\omega_p^2}. \tag{11}$$

One might notice that for our previous condition $C_m \ll C_0$ we find $k_{eff} \ll 1$ and $\omega_s \approx \omega_p$. The resonant frequency relates to the series and parallel frequencies by $\omega_m = (\omega_s + \omega_p)/2$, and therefore a reasonable approximation exists as $\omega_m \approx \omega_s$. This approximation will prove to be beneficial in the next section. Far away from resonance, the device behaves as a capacitor, so its capacitance can be extracted from the admittance curve using the relation $Im(Y_\omega) \to \omega C_0$. As such, running a finite-element simulation of a device and plotting its admittance curve allows us to extract k_{eff}^2 and C_0 for our specific device geometry and inform the equivalent circuit model. Moving beyond the standard BVD model, the modified BVD (mBVD) model includes an additional static resistance R_0 to the static arm of the piezo-mechanical device, which captures the dielectric loss due to energy dissipation in the piezoelectric layer. The mBVD model has been found to more accurately model the behavior of FBAR devices[8], so we use it here. See Appendix A for more details.

B. The Extended BVD model for optomechanical transducers

We can use an extended BVD model to go beyond the piezo-mechanical element and build an equivalent circuit for the entire transducer device, including its optical elements. Using the framework developed by Zeuthen *et al.*[46] and Wu *et al.*[27], we developed an equivalent circuit to model the FBAR transducer. Like the device considered in [27], the FBAR transducer utilizes an optomechanical supermode, where a supermode is formed by the hybridization of two modes that are nearly resonant with each other. In the FBAR transducer, the piezoelectric and mechanical modes are resonant [56], as discussed in Section I A.

The equivalent circuit for a piezo-optomechanical transducer consists of three sub-circuits: the electrical matching network sub-circuit, the piezo-mechanical sub-circuit, and the optical sub-circuit, all of which are coupled together. Thévenin equivalent circuit diagrams are shown in Figures 1 and 3. While we refer the interested reader to references [27, 46] for a detailed derivation of the extended BVD model, we briefly introduce the formalism here.

Before moving on, it's important to clarify an assumption that is made in this work and in previous work on this model [46, 57] : we are assuming the electrical and optical modes are strongly coupled to a single acoustic mode, and weakly coupled to all other acoustic modes. In practice this may not be the case, particularly in unreleased FBAR transducers with a dense forest of acoustic modes with a free spectral range of < 20 MHz [37]. Generalizing the equivalent electrical circuits for transducers with multiple acoustic modes coupled in parallel is an area of potential future exploration.

1. The matching circuit

A matching network (blue sub-circuit in Figures 1, 3) consists of an inductor L, with resistance R_L, and a capacitor C_T coupled to the transducer's acoustic mode via its static capacitance C_0. The matching circuit has a resonant frequency of

$$\omega_{LC} = \frac{1}{\sqrt{L(C_0 + C_T)}} \tag{12}$$

and a quality factor

$$Q_{LC} = \frac{1}{Z_{tx} + R_L}\sqrt{\frac{L}{C_0 + C_T}} \tag{13}$$

with input impedance Z_{tx} from a transmission line. Its linewidth κ_e is

$$\kappa_e = \frac{Z_{tx} + R_L}{L} \tag{14}$$

and its external coupling efficiency η_e is

$$\eta_e = \frac{Z_{tx}}{Z_{tx} + R_L}. \tag{15}$$

For a superconducting circuit, we can set $R_L = 0$. This is a fairly accurate assumption that is explored in detail in Appendix B.

Now that we've defined the matching circuit, we can write an expression for the electromechanical loading of the acoustic mode due to its presence:

$$R_{EM} = Q_{LC}^2 (Z_{tx} + R_L). \tag{16}$$

This loading leads to an electromechanical cooperativity of

$$\mathcal{C}_{EM} = \frac{R_{EM}}{R_m} = \frac{4g_{EM}^2}{\gamma_m \kappa_e} \tag{17}$$

where the electromechanical coupling rate is

$$g_{EM} = \frac{\sqrt{k_T^2}\omega_m}{2} \quad : \quad k_T^2 = \frac{C_m}{C_m + C_0 + C_T}. \tag{18}$$

The electromechanical cooperativity captures the strength of coherent coupling between the electrical and mechanical modes. We can understand the action of the matching network as an impedance transformation provided by the resonant signal enhancement due to its loaded quality factor Q_{LC}. The presence of the electrical LC circuit modifies the resonance condition for the acoustic mode:

$$\omega_m = \sqrt{\frac{1}{L_m}\left(\frac{1}{C_m} + \frac{1}{C_T + C_0}\right)} \tag{19}$$

and, as elsewhere, the presence of the optical mode is assumed not to shift the mechanical resonance [27].

2. The Optomechanical sub-circuit

Next we consider the optomechanical cavity, which is coupled in series to the motional part of the piezo-mechanical element. The optical MRR is understood to have a total linewidth $\kappa_o = \kappa_i + \kappa_{ext}$, where κ_i is its intrinsic linewidth and κ_{ext} is its external coupling rate. The optical external coupling efficiency is given by

$$\eta_o = \frac{\kappa_{ext}}{\kappa_o}. \tag{20}$$

The optomechanical coupling between this optical mode and the mechanical mode is represented by frequency-independent effective resistances $R_{OM,\pm}$. The positive resistance $R_{OM,+}$ represents the desired output mode (upper sideband for direct transduction), and the negative resistance $-R_{OM,-}$ represents the optical noise channel due to the Stokes process creating photons in the lower sideband, which excite spurious phonons in the mechanical mode, creating noise photons in the upper sideband [27].

$$\begin{aligned} R_{OM,+} &= R_m \mathcal{C}_{OM} \mathscr{L}_+^2 \\ R_{OM,-} &= R_m \mathcal{C}_{OM} \mathscr{L}_-^2 \end{aligned} \tag{21}$$

Here $\mathcal{C}_{OM} = \frac{4g_{OM}^2}{\gamma_m \kappa_o}$ is the optomechanical cooperativity and the Lorentzian sideband amplitudes $\mathscr{L}_\pm^2$ are

$$\mathscr{L}_\pm^2 = \frac{(\kappa_o/2)^2}{(\kappa_o/2)^2 + (\omega_m \pm \Delta)^2} \tag{22}$$

where Δ is the detuning of the optical pump from the optical cavity frequency. The optomechanical loading on the acoustic mode is then

$$R_{EM}^{opt} = R_m + R_{OM,+} - R_{OM,-}. \tag{23}$$

Now that we have defined expressions for each sub-circuit of the transducer, let's put the sub-circuits together to characterize the performance of the overall device.

3. Figures of Merit

Given the formalism established above, we can write an expression for the conversion efficiency of the transducer. The conversion efficiency can be written heuristically as

$$\eta = \eta_e \eta_o \eta_{int} \tag{24}$$

where $\eta_{e,o}$ are the external coupling efficiencies of the electrical and optical cavities, respectively, and η_{int} is defined as the internal efficiency of the device. The form of the expression for η_{int} depends on the number of coupled modes comprising the transducer [3]. For a standard optomechanical device with cooperativites $\mathcal{C}_{ij}$, $\mathcal{C}_{jk}$ between modes i, j, k, we write

$$\eta_{int} = \frac{4\mathcal{C}_{ij}\mathcal{C}_{jk}}{(1 + \mathcal{C}_{ij} + \mathcal{C}_{jk})^2}. \tag{25}$$

From our equivalent circuit we can write the appropriate expression for our device:

$$\begin{aligned} \eta &= \eta_e \eta_o \frac{4R_{EM}R_{OM,+}}{(R_m + R_{EM} + R_{OM,+} - R_{OM,-})^2} \\ &= \eta_e \eta_o \frac{4\mathcal{C}_{EM}\mathcal{C}_{OM}\mathscr{L}_+^2}{(1 + \mathcal{C}_{EM} + \mathcal{C}_{OM}(\mathscr{L}_+^2 - \mathscr{L}_-^2))^2}. \end{aligned} \tag{26}$$

While Equation 26 is the commonly cited, or standard, transduction efficiency expression for conversion with one intermediate mode, it only pertains in the low coupling limit, where C_{EM} , $C_{OM} < 1$ [57]. We must take note of this, since the presence of the matching circuit will result in large electromechanical cooperativity $C_{EM} \gg 1$. As such, we must also consider an alternative efficiency expression [57]:

$$\begin{aligned} \eta_{alt} &= \eta_e \eta_o \frac{R_{OM+}}{R_{OM,+} - R_{OM,-} + R_m} \\ &= \eta_e \eta_o \frac{\mathcal{C}_{OM}\mathscr{L}_+^2}{\left(\mathcal{C}_{OM}(\mathscr{L}_+^2 - \mathscr{L}_-^2) + 1\right)} \end{aligned} \tag{27}$$

Equation 27 reflects the fact that $\mathcal{C}_{OM}$ is much smaller than $\mathcal{C}_{EM}$ for our device, and as the bottleneck, it determines the conversion efficiency. In Table II below, we see that for $\mathcal{C}_{EM} > 1$, the standard expression for the efficiency disagrees with the alternative expression. A downside to the alternative expression is its independence from the matching network: according to it, the conversion efficiency does not see a boost from the impedance matching process. As such, we include efficiency estimates from both the standard and alternative expressions in Table II.

From the equivalent circuit we can also extract expressions for added noise during transduction, due to the presence of both optical amplification noise and thermomechanical noise. Optical amplification noise, or Raman noise, occurs when a pump photon produces an output photon at the angular frequency $\omega_{pump} - \omega_m$ via a Stokes process. From two-mode squeezing, this process also produces a phonon which is then transduced into the upper sideband as a noise photon.

$$n_o = \frac{1}{\eta_e}\frac{\mathcal{C}_{OM}\mathscr{L}_-^2}{\mathcal{C}_{EM}} \tag{28}$$

The number of thermo-mechanical noise quanta is given by

$$n_{th} = \frac{1}{\eta_e}\frac{n_m}{\mathcal{C}_{EM}} \tag{29}$$

Here n_m is the thermal bath occupancy given by the Bose-Einstein distribution, $n_m = (e^{\hbar\omega/k_B T} - 1)^{-1}$. The quantity $\mathcal{C}_{EM}/n_m$ is the electromechanical quantum cooperativity. It can be understood as the ratio of coherent electromechanical coupling to the thermal decoherence induced by the mechanical bath, and it reveals how the impedance matching circuit enhances the ratio of electrical signal to mechanical thermal noise in the transducer.

Finally, the conversion bandwidth is given by the dynamically broadened mechanical linewidth:

$$\begin{aligned}\Delta\omega &= \gamma_m(1 + \mathcal{C}_{EM} + \mathcal{C}_{OM}(\mathscr{L}_+^2 - \mathscr{L}_-^2)) \\ &= (R_m + R_{EM} + R_{OM,+} - R_{OM,-})/L_m.\end{aligned} \tag{30}$$

Details of how we modified the extended BVD model to include the static resistance R_0 can be found in Appendix A. Now that we have defined the figures of merit of our transducer as they relate to our model, we can proceed to design an impedance matching network.

4. *Designing the matching network*

It is ideal for all of the figures of merit for our transducer to be optimized simultaneously. In practice, there will be tradeoffs, and devices will have to be designed with use cases and prioritized properties in mind.

Let us begin with the most straightforward goal: optimizing the microwave-to-optical conversion efficiency of the transducer. If we assume the optomechanical and mechanical parameters to be fixed, the signal transfer efficiency expression (Equation 26) reaches its maximum as a function of C_{EM} when

$$\mathcal{C}_{EM} = \mathcal{C}_{EM}^{opt} = 1 + \mathcal{C}_{OM}(\mathscr{L}_+^2 - \mathscr{L}_-^2). \tag{31}$$

To satisfy the cooperativity relationship in Equation 31 we need to choose the matching circuit parameters C_T, L, such that the electromechanical loading R_{EM} is equal to the optomechanical loading R_{EM}^{opt}[27]:

$$R_{EM} = R_m + R_{OM,+} - R_{OM,-}. \tag{32}$$

This amounts to choosing the electromechanical broadening of the mechanical mode to be equal to the intrinsic mechanical linewidth plus the net optomechanical broadening. Working through the algebra, this relationship leads us to two equations for the matching circuit that we must solve in accordance with the resonance condition $\omega_{LC} = \omega_m$:

$$C_T = \frac{1}{\omega_m}\sqrt{\frac{1}{R_{EM}^{opt}(Z_{tx} + R_L)}} - C_0 \tag{33}$$

$$L = \frac{1}{\omega_m}\sqrt{R_{EM}^{opt}(Z_{tx} + R_L)}. \tag{34}$$

This system of equations must be solved self-consistently. However, an analytical solution of Equations. 33 and 34 may be obtained if we assume that the dependence of R_{EM}^{opt} on the acoustic mode frequency ω_m can be neglected. This is a valid assumption when $k_{eff}^2 \ll \kappa_o/\omega_s$ [27]. For the transducer, $k_{eff}^2 = 4.3 \times 10^{-3}$ and $\kappa_o/\omega_s = 4.566 \times 10^{-2}$, so we can proceed with this approximation. For the analytical solution at the resonance condition $\omega_{LC} = \omega_m$, with the earlier assumption $\omega_m \approx \omega_s$ and

$$\omega_s \equiv \sqrt{\frac{1}{L_m C_m}}, \tag{35}$$

the new expression for C_T takes the form [27]

$$C_T = \frac{C_m}{2}\left[\sqrt{1 + \frac{4}{R_{EM}^{opt}\omega_s^2 C_m^2(Z_{tx} + R_L)}} - 1\right] - C_0 \tag{36}$$

where the matching inductance can now be calculated via

$$L = \frac{L_m C_m(C_0 + C_T)}{(C_0 + C_T)(C_m + C_0 + C_T)} = \frac{1}{\omega_s^2(C_m + C_0 + C_T)}. \tag{37}$$

How do these expressions change when we wish to minimize the added noise during transduction? When this is our goal over and above efficiency maximization, we turn away from impedance matching as commonly understood. Here, we no longer wish to achieve zero signal reflection on resonance ($\omega_m = \omega_{LC}$). Instead, we want to maximize the electromechanical cooperativity $\mathcal{C}_{EM}$ to minimize the number of thermal noise quanta (Equation 29). Since $\mathcal{C}_{EM}$ is inversely proportional to the matching capacitance, we can simply set $C_T = 0$, and calculate the matching inductance L at the resonant condition as is done to maximize conversion efficiency.

Detailed derivations behind this brief summary section can be found in reference [27]. In Sec. II D below, we use this formalism to design impedance matching networks for FBAR transducers. Before detailing these results, we must ask, can the formalism be modified to include an additional cooperativity? If so, how? Such a modification is necessary for transducers that utilize two coupled optical cavities. We explore this question next.

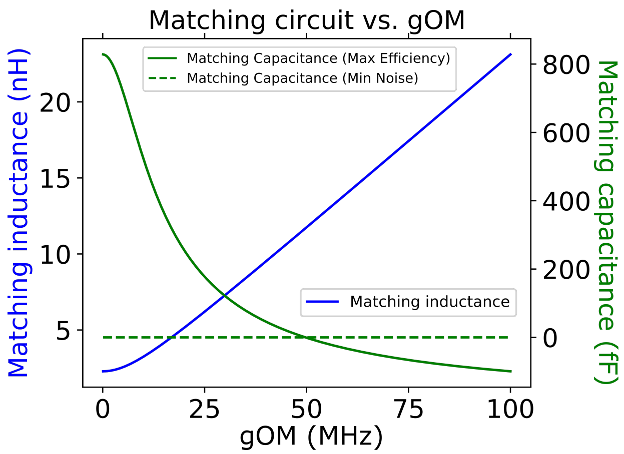

FIG. 4. Matching inductance (blue) and capacitance (green) for a single-ring FBAR transducer as a function of g_{OM}. The matching inductance is the same for efficiency maximization and noise minimization, and increases linearly for $g_{OM} > 3$ MHz. For a noise-minimizing circuit, the matching capacitance is constant at zero. For an efficiency-maximizing circuit, the matching capacitance decreases with increasing g_{OM}. The formalism outputs a negative (un-physical) matching capacitance for $g_{OM} > 50$ MHz.

C. Modifying the equivalent circuit to incorporate a photonic molecule

Here we modify the extended BVD model to include the optomechanical loading from a photonic molecule, i.e. a system of two coupled micro-ring resonators, for the first time. A photonic molecule is a two-level photonic system that can be dynamically controlled by gigahertz-frequency microwave signals, and it typically consists of two coupled MRRs, where only one MMR is coupled to a bus waveguide [58]. This extension is a crucial step for modeling a wide range of optomechanical transducers, since many rely on the mode splitting within a photonic molecule to achieve triply resonant transducer operation [38]. When two MRRs are coupled at a rate J, their modes hybridize into supermodes. So-called symmetric and anti-symmetric supermodes appear with a frequency splitting equal to $2J$. For microwave-to-optical transduction, the optical pump is tuned to the lower-frequency symmetric supermode frequency ω_s, which sits $\omega_m = 2J$ lower than ω_A. This triply-resonant condition, when satisfied, should boost the conversion efficiency at a given optical power due to the cavity enhancement of the pump tone [38].

TABLE I. Input Parameters for Extended BVD Model.

Name	Symbol	Value
Single photon optomechanical coupling rate	$g_{OM,0}/2\pi$	400 Hz
Optical cavity frequency	$\omega_o/2\pi$	193 THz
Optical intrinsic linewidth	$\kappa_i/2\pi$	25 MHz
Optical external coupling rate	$\kappa_{ext}/2\pi$	125 MHz
Mechanical mode frequency	$\omega_m/2\pi$	3.285 GHz
Mechanical intrinsic linewidth	$\gamma_i/2\pi$	2.6 MHz
Electromechanical coupling factor	k^2_{eff}	4.3E-3
Optical Cavity Photon Number	n_{cav}	$1E6 - 2.5E9$
Static capacitance	C_0	200 fF
Static resistance	R_0	10 $k\Omega$
Device Temperature	T	10-100 mK
Ring-ring coupling rate	$J/2\pi$	1.7 GHz

The coupling between the two MRRs introduces additional optomechanical loading on the mechanical mode, so we must re-define the equivalent optomechanical circuit for this device. We do this by adding two additional resistors $R_{OO,\pm}$ to represent the optical signal and noise outputs, and add these in parallel with a modified optomechanical coupling resistor R_{OM}. $R_{OO,\pm}$ are added in parallel, as opposed to in series, following the generic formalism put forth in Ref. [57]. The addition of a second MRR, and the corresponding optical-optical cooperativity $\mathcal{C}_{OO}$, transforms the device from a 1-stage transducer to a 2-stage transducer. As such, the effective electrical circuit renders the correct transmission coefficient for the device within the Heisenberg-Langevin equations of motion [57].

The coupling between the acoustic mode and the first optical cavity is now represented by the effective impedance R_{OM} as

$$R_{OM} = R_m \mathcal{C}_{OM}. \tag{38}$$

This term now represents the optomechanical interaction without including information about the output sideband amplitudes. To capture that information, we add in two resistive terms. The resistors $R^{\pm}_{OO}$ are defined as

$$\begin{aligned} R_{OO,+} &= R_m \mathcal{C}_{OO} \mathscr{L}_+^2 \\ R_{OO,-} &= R_m \mathcal{C}_{OO} \mathscr{L}_-^2 \end{aligned} \tag{39}$$

For the newly defined optical-optical cooperativity $\mathcal{C}_{OO}$

$$\mathcal{C}_{OO} = \frac{4J^2}{\kappa_1 \kappa_2} \tag{40}$$

where we assume the intrinsic linewidths of both cavities are equal, $\kappa_1 = \kappa_2 = \kappa_o$, and J is the ring-ring coupling rate. These terms include the information about Anti-Stokes and Stokes output sideband amplitudes. We note that, while these changes to the equivalent circuit modify the expressions for the optomechanical circuit elements, they do not change the expressions for the piezoelectric sub-circuit or impedance matching network elements.

For analysis of the circuit, we add the optomechanical resistors together in parallel, yielding the expression

$$R_{OM}^{eq} = \left(\frac{1}{R_{OM}} + \frac{1}{R_{OO,+} - R_{OO,-}}\right)^{-1}$$
$$= R_{OM,+}^{eq} - R_{OM,-}^{eq} = \frac{R_{OM}(R_{OO,+} - R_{OO,-})}{R_{OM} + R_{OO,+} - R_{OO,-}}$$
$$= R_m \mathcal{C}_{OM}^{eq}(\mathscr{L}_+^2 - \mathscr{L}_-^2) \quad (41)$$

where the modified optomechanical cooperativity is defined as

$$\mathcal{C}_{OM}^{eq} = \frac{\mathcal{C}_{OM}\mathcal{C}_{OO}}{\mathcal{C}_{OM} + \mathcal{C}_{OO}(\mathscr{L}_+^2 - \mathscr{L}_-^2)}. \quad (42)$$

And the optomechanical loading on the acoustic mode is now

$$R_{EM}^{opt} = R_m + R_{OM}^{eq}. \quad (43)$$

What expressions should we use to extract the device's figures of merit now? The expression for thermal noise remains unchanged (see Equation 29), but the expressions for Raman noise, conversion efficiency and bandwidth do change. The optical Raman noise is now

$$n_o = \frac{1}{\eta_e}\frac{\mathcal{C}_{OM}^{eq}\mathscr{L}_-^2}{\mathcal{C}_{EM}}, \quad (44)$$

the bandwidth is defined as

$$\Delta\omega = \gamma_m(1 + \mathcal{C}_{EM} + \mathcal{C}_{OM}^{eq}(\mathscr{L}_+^2 - \mathscr{L}_-^2))$$
$$= (R_m + R_{EM} + R_{OM}^{eq})/L_m \quad (45)$$

so we see that the additional optomechanical loading further broadens the conversion bandwidth. What of the efficiency? Following the standard expression, which applies when $\mathcal{C}_{OM}, \mathcal{C}_{EM}, \mathcal{C}_{OO} < 1$, we write

$$\eta = \eta_e\eta_o\frac{4R_{EM}R_{OM,+}^{eq}}{(R_m + R_{EM} + R_{OM}^{eq})^2}$$
$$= \eta_e\eta_o\frac{4\mathcal{C}_{EM}\mathcal{C}_{OM}^{eq}\mathscr{L}_+^2}{(1 + \mathcal{C}_{EM} + \mathcal{C}_{OM}^{eq}(\mathscr{L}_+^2 - \mathscr{L}_-^2))^2}. \quad (46)$$

However, for the two-ring device, we are far outside of the low-cooperativity regime. The strong ring-ring coupling needed to achieve supermode splitting at relevant frequencies of 4 GHz results in large $\mathcal{C}_{OO}$, and consequently, the matching circuit yields a large $\mathcal{C}_{EM}$. For $\mathcal{C}_{EM} \gg \mathcal{C}_{OM}$, $\mathcal{C}_{OO} \gg \mathcal{C}_{OM}$, we must also consider the alternative expression [59]:

$$\eta_{alt} = \eta_e\eta_o\frac{\mathcal{C}_{OM}}{(\sqrt{\mathcal{C}_{OM} + 1} + 1)^2}$$
$$= \eta_e\eta_o\frac{R_{OM}}{(\sqrt{R_{OM} + R_m} + \sqrt{R_m})^2} \quad (47)$$

as with the 1-ring transducer, the alternative efficiency expression has no dependence on the matching circuit. We include both the standard and alternative efficiency values in Table II.

D. Matching circuits for single-ring and double-ring FBAR transducers

Here we apply the above formalism to the design of matching circuits for FBAR transducers. For all calculations, we use physical parameters from Blesin *et al.*[26] as inputs to the model: these parameters are listed in Table I. For all calculations, we also set the device temperature to 50 mK and the cavity-enhanced optomechanical coupling rate to 10 MHz, which corresponds to 6.25×10^8 photons in the optical cavity. The frequency of the optical pump is set to be red-detuned from the optical cavity mode by the acoustic mode frequency: $\Delta_o = -\omega_m$. Results obtained for single- and double-ring devices are summarized in Table II and discussed briefly here.

1. Matching Circuit for Single-Ring FBAR Transducer

The matching capacitance and inductance values required for a single-ring FBAR transducer are plotted versus g_{OM} in Figure 4. The plot shows how the required matching capacitance increases versus pump power for an efficiency-maximizing circuit. At $g_{OM} > 50$ MHz, the matching capacitance becomes negative. This unphysical result tells us that it is not possible to design an efficiency-maximizing impedance matching circuit at this pump power. The matching inductance is equal for either efficiency maximization or noise minimization, and increases with pump power. Overall, this plot shows that it is easier to fabricate matching circuits for lower pump power operation of the transducer.

An impedance matching circuit designed to maximize conversion efficiency at a moderate pump power with $g_{OM} = 10$ MHz requires a matching capacitance of 522.346 fF and a matching inductance of $L =$ 3.246 nH. This circuit results in a conversion efficiency of 42.197%. Since all cooperativities have values close to 1, the standard efficiency expression matches the alternative efficiency expression. The conversion bandwidth is 10.533 MHz, the Raman noise quanta are 6.598×10^{-5} per transduced photon, and the thermal noise quanta are $2.203 - 2 \times 10^{-2}$ per transduced photon.

When we modify the matching circuit to minimize added noise, $C_T \rightarrow 0$ fF, the required matching inductance remains almost the same. With this matching circuit, we achieve a conversion efficiency of 28.688% (standard expression). The decrease in efficiency is to be expected, since the matching circuit no longer minimizes signal reflections when $\omega_{LC} = \omega_m$. We add 1.829×10^{-5} Raman noise quanta per transduced photon, and 6.110×10^{-3} thermal noise quanta per transduced photon. Choosing this circuit, we can lower the thermal noise quanta by 27.7%. In the process, we sacrifice conversion efficiency. Using the standard efficiency expression,the efficiency drops - however, $\mathcal{C}_{EM} = 7.304 > 1$, outside of the low-cooperativity regime where the standard expression applies - so we must be wary of this

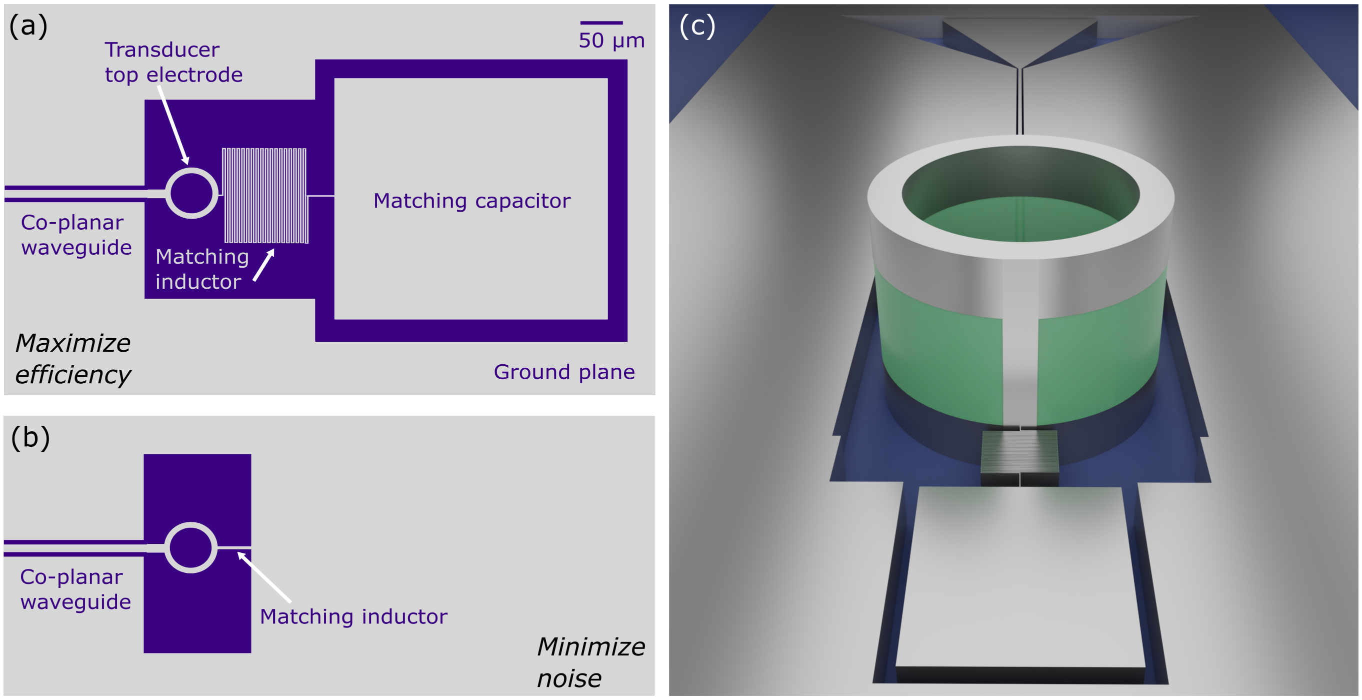

FIG. 5. Example device designs for a single-ring FBAR transducer. The matching networks shown here are qualitatively designed for an FBAR transducer with the properties listed in Table I and $g_{OM} = 10$ MHz. The matching network depicted in (a,b) is designed to maximize the conversion efficiency of the transducer, and consists of a meandering inductor and a square-shaped capacitor. The 3D rendering in (b) shows an electrical wirebonding pad leading to a 50 Ohm superconducting waveguide, which is galvanically connected to the transducer. The green layer in (b) is the AlN piezo layer. Not shown here is the piezo cavity's bottom electrode and the cladded MRR, sitting beneath the piezo cavity. The device depicted in (c) has a matching network designed to minimize added noise, which consists of a high kinetic inductance nanowire inductor. The design is similar for double-ring devices: a second optical ring resonator would be coupled to the ring located beneath the top electrode shown. Note that (a,b) show a MRR with a radius of 20 μm to match reference [26], whereas (c) has a MRR radius of 125 μm to match reference [37].

value. The alternative efficiency value (42.197%) doesn't change, since it does not depend on matching circuit parameters. We can then understand the peak conversion efficiency to sit in a band between these upper and lower bounds, understanding the efficiency is likely to be lower than that for the efficiency-maximizing matching network.

The optimal matching circuit values depend sensitively on the operating regime of the transducer. For example, for $g_{OM} = 10$ MHz, the matching capacitance to optimize conversion efficiency is 522 fF. If we increase the number of optical pump photons from 6.25×10^8 to 2.5×10^9, a four-fold increase, the optimal matching capacitance falls to 253 fF. These results reinforce the requirement to design and fabricate transducers to operate within a specific set of experimental conditions, informed by the resulting estimated figures of merit entanglement protocols, as we obtain below. See Fig. 5 for an example impedance-matched transducer design.

When designing impedance matching networks, especially those that require $C_T = 0$ to minimize added noise, we must take care to consider the effects of parasitic capacitance terms. Spiral inductors, like the one depicted in Ref. [27], have significant self-capacitances and capacitances to ground. If ignored, stray capacitances will pull the matching circuit away from its optimal regime, leading to degraded device performance. Likewise, matching capacitors will have parasitic inductances. In Appendix C we investigate the effects of these unwanted terms on the matching network and transducer performance.

2. *Matching Circuit for Double-Ring FBAR Transducer*

For a two-ring transducer, the matching circuit must be designed to match the new optomechanical subcircuit. Of note, adding the new resistors $R_{OO,\pm}$ in parallel with R_{OM} only changes the total optomechanical loading very minimally, from 90.314 Ω to 90.229 Ω. Because of the similar optomechanical loading, the matching circuit values and corresponding figures of merit are similar for both instantiations of the device, both for efficiency-maximizing and noise. The only notable difference is that the alternative efficiency expressions for the two-ring device return a lower efficiency value. It appears that for the single ring devices, the appropriate standard expres-

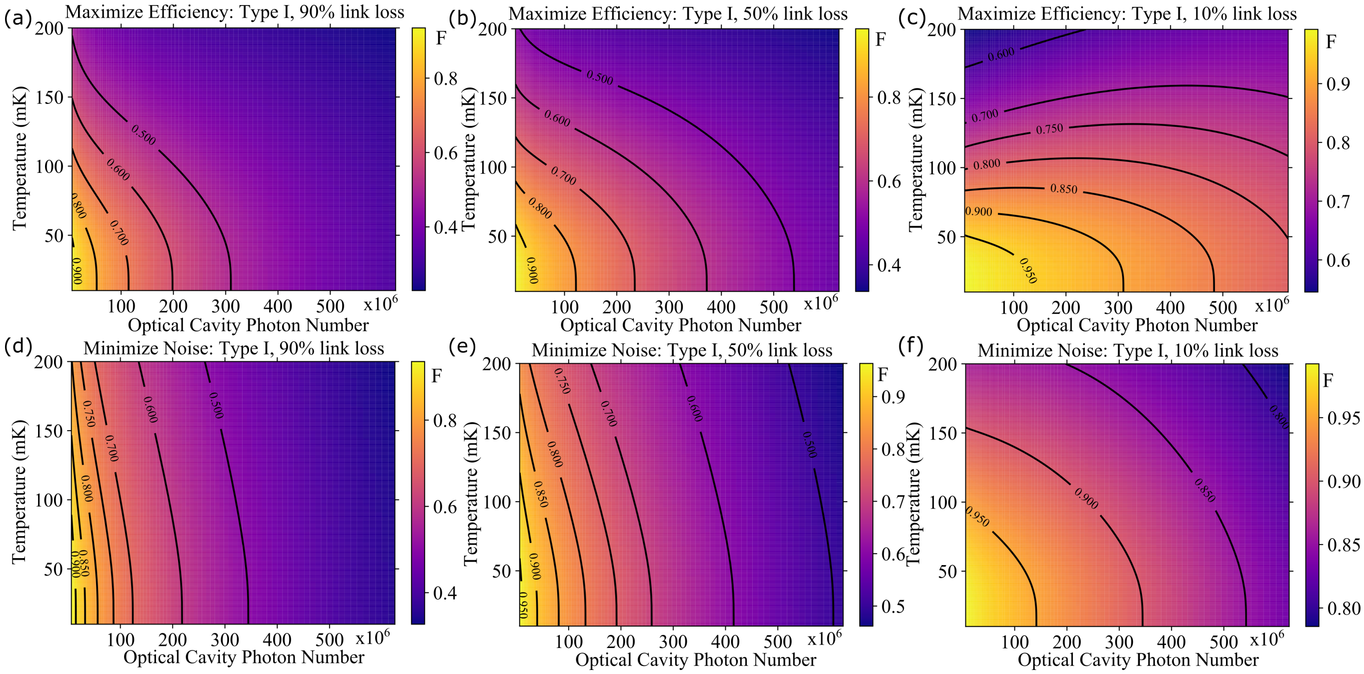

FIG. 6. Entanglement readout fidelity F for Type-I heralding protocols plotted versus optical cavity photon number and device temperature. The plots are shown with link loss values of 90% (a,b), 50% (c,d) and 10% (e,f). These results show that the achievable readout fidelity has a strong dependence on η_l, which is mitigated to a small degree using noise-minimizing matching circuits. Overall, the achievable fidelity is boosted by at least 5%, and up to 10% or more, at higher temperatures when the noise-minimizing matching circuit is used.

sion overestimates the conversion efficiency, whereas for the two-ring device, the appropriate standard expression underestimates the efficiency.

While the matching circuits for one-ring and two-ring transducers are similar for the operating regime studied here, we are now equipped with a more generalized formalism that enables us to design matching networks across a wider variety of optomechanical transducers. One such design is discussed below.

3. *Example Matching Circuit Design*

Using the above formalism, we here propose device designs for FBAR transducers with both efficiency-maximizing and noise-minimizing matching circuits. Rough order-of-magnitude qualitative designs and renderings for these devices are shown in Fig. 5, where the FBAR transducer is understood to have the material stack shown in the cross-section in Fig. 1(a). The device shown here has a MRR with a radius of 20 μm, (125 μm in panel (c)), and an annulus-shaped top electrode. The electrode is fabricated using a pull-back process [38, 60] engineered to minimize electrode capacitance. This is a qualitative diagram, and the design is understood to be applicable to a variety of optical cavities and electrode configurations.

The example designs are shown with a 200 nm thick Niobium superconducting layer, which defines the superconducting circuit and the ground plane. A wire-bonding pad (top of panel (b)) connects to a 50 Ohm superconducting waveguide, which connects galvanically to the top electrode of the transducer. This electrode is also galvanically connected to the impedance matching circuit to achieve the in-parallel configuration dictated by the extended BVD circuit model. The ground plane for the impedance matching circuit is the same as the ground of the transducer's piezo cavity. The efficiency-maximizing version of the impedance matching network shown in panel (a,b) incorporates a Niobium meandering inductor. The total footprint is an area of approximately 100 μm $\times$ 100 μm. The meander line width, center-to-separation, and total length should be designed to target a total inductance in the $2-4$ nH range with an anticipated parasitic capacitance in the $5-10$ fF range. The specific lumped element values will depend on the quality of the deposited materials and fabrication conditions, so this example is meant to be qualitiative and not exact. The matching capacitor is designed in a rectangular shape with dimensions of approximately 300 μm $\times$ 325 μm, and has an additional capacitance of $400-500$ fF.

A device with a noise-minimizing version of the matching network is shown in panel (c). Since this matching network requires a capacitance as close to zero as possible, the square capacitor is discarded and the meandering inductor is swapped out for a high kinetic inductance nanowire inductor [61]. The nanowire inductor shown

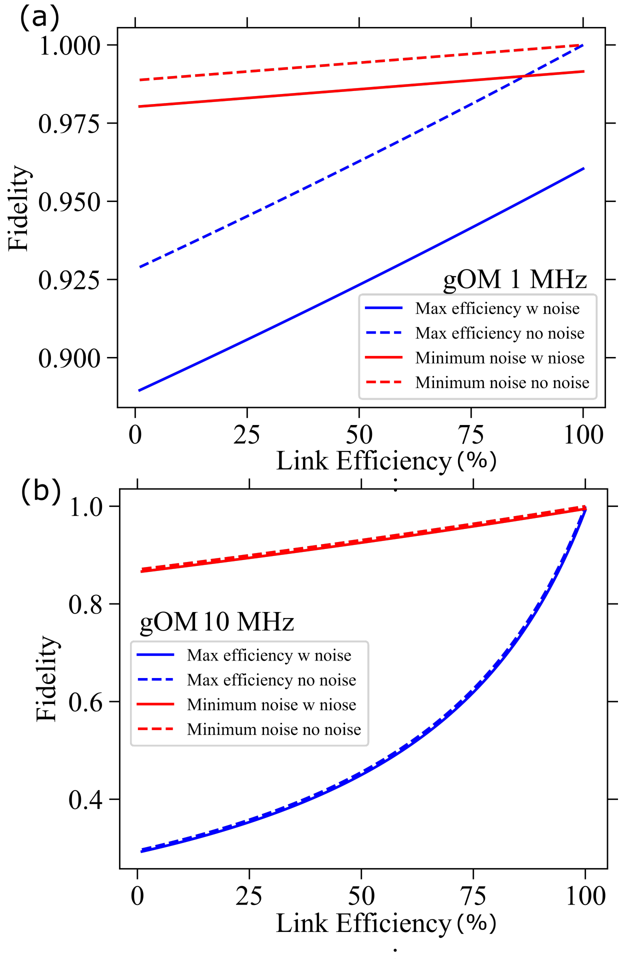

FIG. 7. Type-I Entanglement readout fidelity versus link loss for $T = 50$ mK and (a) $g_{OM} = 1$ MHz and (b) $g_{OM} = 10$ MHz. Blue curves correspond to efficiency-maximizing matching circuits and red curves correspond to noise-minimizing matching circuits. Dashed curves correspond to fidelity ignoring the effects of thermal noise, and solid curves take thermal noise into account. For larger g_{OM}, the difference in fidelity between the two matching circuits is more prominent, since the probability of false positive detection events increases more dramatically for high link loss.

consists of a ~ 20 nm-thick NbN layer with a width of 1 μm and length of ~ 150 μm. Depending on the specific materials and fabrication recipes involved, the nanowire length can possibly be reduced to < 10 μm to achieve an inductance in the $2 - 4$ nH range with an estimated parasitic capacitance is in the aF range. Additional discussion exploring the effects of parasitic lumped element terms can be found in Appendix C.

III. BVD-INFORMED ENTANGLEMENT HERALDING PROTOCOLS

Now that we have established how to design impedance matching networks for the FBAR transducer, both to

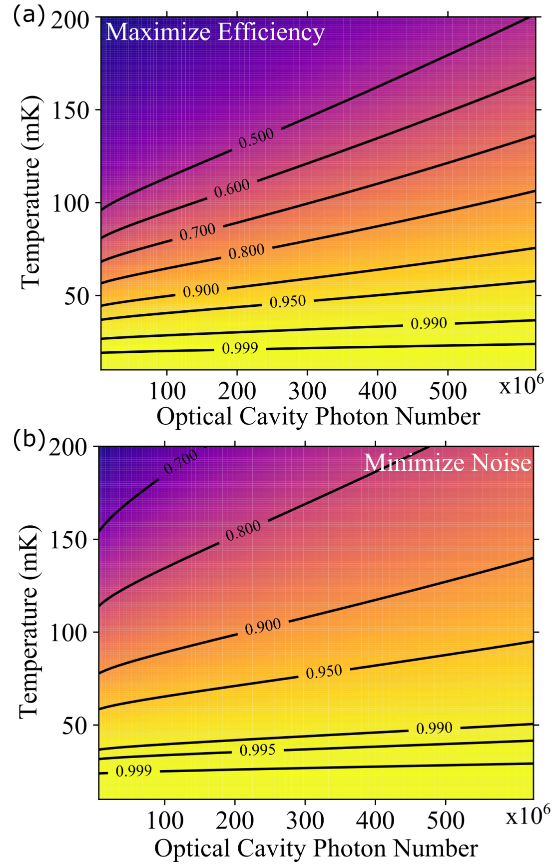

FIG. 8. Type-II Entanglement fidelity F versus temperature and optical cavity photon number for a matching circuit (a) maximizing conversion efficiency and (b) minimizing added noise. The Type-II protocol is not susceptible to lower fidelities at higher pump powers, as opposed to the Type-I protocol. The addition of a noise-minimizing impedance matching circuit in (b) significantly improves fidelity as the temperature increases.

maximize conversion efficiency and minimize added noise, we investigate how the impedance-matched devices perform within Type-I and Type-II entanglement heralding protocols. Readout fidelities and entanglement generation rates are plotted and analyzed in various experimental operating conditions. These results allow us to make informed decisions in the device design phase to optimize the chosen quantum networking protocol, given a set of realistic experimental parameters such as temperature, transducer pump power, and link loss between the transducer and the Bell state analyzer.

Let us begin with Type-I entanglement heralding. Because this is a single-photon protocol, it will succeed only when one photon is emitted, in total, from both network nodes (see Fig. 2). For each trial of the experiment, there is a small chance that both superconducting network nodes will produce an entangled telecom photon, and that one of these photons will be lost in the network before reaching the photodetector. Instances such as these, where two photons are emitted but only one is detected, and the two events are completely uncorrelated, produce false positive events and contribute to the infidelity. In conceiving false positive detection events this way, we are assuming that two-photon detection events can be sorted from one-photon detection events and discarded through post-selection.

While this source of infidelity is limiting, in practice, the primary downside of Type-I entanglement is the requirement of absolute relative phase stability between the photon sources and the beamsplitter [48]. Slight changes in optical fiber path length due to temperature fluctuations, for example, can change the relative phase of the entangled state. This approach could still be suitable for entanglement generation between cryostats in the same building, e.g. local area networks, but will quickly become untenable for longer networks with larger inherent phase instabilities. In the discussion below, the fidelity, or readout fidelity, of the protocol refers to the conditional fidelity of Bell state generation [28], that is, the overlap of the created quantum state with the desired quantum state, given that the relevant photodetector click condition is fulfilled.

Wang *et al.* developed a framework to extract the fidelity and entanglement generation rate of a heralding protocol that depends on the properties of an optomechanical transducer[59], but did not incorporate contributions from added noise. Zeuthen *et al.* developed expressions for entanglement fidelity in the presence of noise [28] and found that the fidelity depends much more sensitively on the number of added noise quanta than on conversion efficiency. Here, we combine the methods of [28, 59] while establishing a connection to the extended BVD model for an impedance-matched transducer.

Assuming a Poissonian photon detection process, following the Stochastic master equation [12], a photon is emitted by the transducer with probability

$$P_1 = 1 - P_0 = 1 - e^{-r_o \Delta t} \tag{48}$$

where r_o is the photon generation rate and Δt is the fixed time duration of the transduction process. Note that Eq. 48 represents the probability that *at least* one photon is emitted, and not precisely one photon. The probability of precisely one photon emission event occurring within Δt is

$$P_{single} = r_o \Delta t e^{-r_o \Delta t}. \tag{49}$$

$P_1 \approx P_{single}$ when $P_1 \ll 1$, i.e. when the product $r_0 \Delta t <$ 1. As will be shown below (see Table III), we obtain the values at or near $r_0 \Delta t = 0.28$ at a relatively high optomechanical coupling rate of 10 MHz. For this value, $P_1 \approx P_{single}$. We must remain aware of this assumption, however, understanding that it becomes less accurate as the pump power to the transducer is increased.

Next we define the expression for Δt. For an FBAR transducer with a single optical cavity, we have the transduction time duration

$$\Delta t = 2\pi \left({}^1/_{g_{EM}} + {}^1/_{g_{OM}} + {}^1/_{\kappa_{ext}} \right) \tag{50}$$

which can be understood as the sum of the lifetimes of each of the constituent cavity modes of the device, plus the time it takes for a transducer photon to couple out of the MRR and into the optical bus waveguide. For a two-MRR transducer we have

$$\Delta t_{2MRR} = 2\pi \left({}^1/_{g_{EM}} + {}^1/_{g_{OM}} + {}^1/_{J} + {}^1/_{\kappa_{ext}} \right). \tag{51}$$

Both single-MRR and double-MRR devices have an optical photon generation rate (for a single microwave photon input) of

$$r_o = \frac{1}{2\pi} \frac{4 g_{OM}^2 \kappa_{ext}}{(\kappa_{ext} + \kappa_i)^2} \tag{52}$$

where κ_{ext} is the external coupling rate of the optical cavity, and κ_i is its intrinsic loss rate. The probability of successfully detecting an emitted photon is

$$P_{succ} = P_1 \eta_l \eta_{det}. \tag{53}$$

Where η_l is the probability that the photon reaches the photodetector without being lost in the network link, and η_{det} is the detector efficiency.

The desired, or target, photonic Bell state is

$$|\Psi_{phot}\rangle = \sqrt{P_{01}}\, |0_A 1_B\rangle + \sqrt{P_{10}}\, |1_A 0_B\rangle \tag{54}$$

where P_{01} (P_{10}) is the probability that Node A(B) emits zero photons and Node B(A) emits one photon

$$P_{01} = P_{10} = P_1 P_0 = (1 - e^{-r_o \Delta t}) e^{-r_o \Delta t}. \tag{55}$$

The detection of the target photonic Bell state after the beamsplitter will project the remote superconducting circuits into the distributed Bell state

$$|\Psi_{SQ}\rangle = \sqrt{P_{01}}\, |e_A g_B\rangle + \sqrt{P_{10}}\, |g_A e_B\rangle \tag{56}$$

where $|g\rangle$, $|e\rangle$ are the qubits' ground and excited states, respectively. During an entanglement generation attempt, there is a probability that both network nodes will emit entangled photons, but one photon is lost before reaching the photodetector. This scenario contributes false positive events to the infidelity of the protocol, since both superconducting qubits will be in their ground states, even though we think one is in its excited state. This occurs with P_{in}, the probability of an infidelity-causing event, of approximately

$$P_{in} = P_{11} \eta_l (1 - \eta_l) = P_1^2 \eta_l (1 - \eta_l). \tag{57}$$

As such, the fidelity of the protocol is then:

$$F = \frac{P_{01}\eta_l + P_{10}\eta_l}{P_1^2 \eta_l (1 - \eta_l) + P_{01}\eta_l + P_{10}\eta_l} = \frac{2P_{01}}{P_1^2 (1 - \eta_l) + 2P_{01}}. \tag{58}$$

In other words, the fidelity is equal to the ratio of the total probability of creating the desired state to the sum of the probabilities of creating the desired state and of creating an undesired state with a single detection event. As the pump power to the transducers increases, P_1^2 increases, and the fidelity is degraded. Note that by counting false positive events in this manner, we assume that we are able to distinguish between single count events (desired) and coincident events (undesired) and discard those through post-selection. The associated photon generation rate is

$$n_r = 2r_0 e^{-r_0 \Delta t} \left(\frac{\Delta t}{\Delta t + t_r} \right) \tag{59}$$

for a superconducting qubit reset time t_r. The factor of 2 is present because either node can emit a photon. This leads to an entanglement generation rate of

$$\tau_{ent} = n_r \eta_l \eta_{det}. \tag{60}$$

A. Incorporating Infidelity Contributions Due to Thermal Noise

For a thermal population of n_{th}, the probability of the transducer emitting a photon due to this thermal occupation is approximately

$$P_{th} = 1 - e^{-r_{th} \Delta t} \tag{61}$$

where r_{th} is the rate of photon generation due to the presence of thermal quanta in the transducer's acoustic mode:

$$r_{th} = r_o n_{th}. \tag{62}$$

The expression for the infidelity is now

$$\begin{aligned} P_{in} = [&P_1^2(1 - P_{th})^2 + \\ &P_{01} P_{th}(1 - P_{th}) + \\ &P_{10} P_{th}(1 - P_{th}) + \\ &P_{00} P_{th}^2]\eta_l(1 - \eta_l) + \\ &2P_{th}(1 - P_{th}) P_{00} \eta_l. \end{aligned} \tag{63}$$

The $(P_{01}P_{th}(1 - P_{th}) + P_{10}P_{th}(1 - P_{th}))\eta_l(1 - \eta_l)$ terms correspond to false positive events arising from attempts where one node emits a photon entangled with a superconducting qubit, and the other node emits a photon due to the presence of thermal quanta in the transducer, and one of the photons is lost before reaching the photodetectors. The $P_{00}P_{th}^2\eta_l(1 - \eta_l)$ term corresponds to false positive events arising from attempts where both nodes emit photons due to the presence of thermal quanta in the transducer and one of the two emitted photons is lost before hitting the photodetector. There is an additional term of $2P_{th}(1 - P_{th})P_{00}\eta_l$ which represents false positive events arising from attempts where neither node emits an entangled photon, but one node emits a photon due to thermal excitation, and that photon reaches a photodetector.

If nodes A and B emit photons with the same probability ($P_{01} = P_{10}$), this simplifies to

$$\begin{aligned} P_{in} = [P_1^2(1-P_{th})^2 + 2P_{01}P_{th}(1-P_{th}) + P_{00}P_{th}^2]\eta_l(1-\eta_l) + \\ 2P_{00}P_{th}(1 - P_{th})\eta_l \end{aligned} \tag{64}$$

The fidelity expression takes the form

$$\begin{aligned} F &= \frac{2P_{01}(1 - P_{th})^2\eta_l}{P_{in} + 2P_{01}(1 - P_{th})^2\eta_l} \\ &= \frac{2P_{01}(1 - P_{th})^2}{(P_1^2(1 - P_{th})^2 + 2P_{01}P_{th}(1 - P_{th}) + P_{00}P_{th}^2)(1 - \eta_l) + 2P_{00}P_{th}(1 - P_{th}) + 2P_{01}(1 - P_{th})^2}. \end{aligned} \tag{65}$$

Here is the point where the extended BVD model of our transducer comes into play. For a given set of device and operating parameters, the BVD model outputs matching circuit parameters, an estimated conversion efficiency, and estimates for added noise quanta due to Raman and thermal noise. (Note that in this section we disregard Raman noise quanta, since there are multiple orders of magnitude fewer noise quanta due to Raman noise.) We can use the thermal noise output (Equation 29) from the BVD model as an input to our entanglement generation fidelity expressions, while simultaneously optimizing our transducer for either highest-efficiency or lowest-noise operation. To do this, we input the BVD value of n_{th} into Equation 62.

B. Two-Photon Protocol with Thermal Noise

Type-II entanglement heralding involves the interference of two optical photons, one emitted from each node. The interferometric phase is now common to both photons. As such, it can be factored out of the distributed entangled state, bypassing strict requirements on phase stability. Not only are Type-II entanglement protocols more robust to instabilities due to path-length variations, they are also not limited by the intrinsic contribution to the infidelity described for Type-I above, where two photons are emitted but one is lost. This means that the quantum memories can be pumped harder to emit photons with a higher probability.

For these protocols, the quantum information can be stored in the frequency, state of polarization, or time-bin degree of freedom of the optical photon [48]. Since superconducting qubits will most naturally emit time-bin encoded photons[62, 63], we focus on the time-bin encoding basis for qubit-photon entanglement. Time-bin encoding is commonly found in color-center based quantum networking experiments [64, 65].

Here, for example, detecting a photon in the Early time bin mode corresponds to a qubit in its ground state, whereas a photon in the Late time bin mode corresponds to a qubit in its excited state. Changing to the time-bin basis, the target photonic Bell state is now

$$|\Psi_{phot}\rangle = \sqrt{P_{A,L}P_{B,E}}\,|0_E 1_L\rangle - \sqrt{P_{A,E}P_{B,L}}\,|1_E 0_L\rangle \tag{66}$$

where $P_{A,L}$ is the probability that Node A emits a photon in the Late time bin and $P_{B,E}$ is the probability that Node B emits a photon in the Early time bin. If this photonic state is detected, it will project the superconducting qubits into the target Bell state

$$|\Psi_{SQ}\rangle = \sqrt{P_{eg}}\,|eg\rangle - \sqrt{P_{ge}}\,|ge\rangle \tag{67}$$

where $P_{eg} = P_{A,L}P_{B,E} = P_1^2$ is the probability that the qubit at Node A is in the excited state and the qubit at Node B is in the ground state.

Let us now formulate expressions for the fidelity of the two-photon entanglement heralding protocol. Entanglement attempts that produce zero or one photons instead of two can be discarded: this post-selection process is powerful in that it avoids many would-be sources of infidelity that do not produce one click each in the Early and Late time bins. We are free to increase the pump power to the transducer without worrying about two-photon emission events. Following our reasoning for the fidelity expression in Equation 58, there are no sources of infidelity in the absence of noise. This will not be the case for realistic experimental conditions, but, seeing as state preparation for superconducting qubits is a high-fidelity operation, we assume as much here.

As we will discover, the presence of thermal excitations in the transducer's acoustic cavity contribute more significantly to the infidelity for the Type-II protocol, as compared to the Type-I protocol. This result may seem counter-intuitive; however it is the case, because the time-bin Type-II protocol allows more opportunities for spurious photon emission events to produce the desired click condition and generating false positive events, as detailed below.

There are two sets of false positive events to consider in the presence of thermal noise: first, for each entanglement attempt, it may happen that one node emits an entangled photon in one time bin, whereas either node emits a photon in the opposite time bin due to the presence of thermal quanta in the transducer. There are eight such contributions, two each from the four combinations of Early/Late signal photon emission: for each combination, either node may emit the noise photon. Here we note that a single node can emit in *both* of the time bins as a result of thermal noise. This situation obtains when the time bin separation t_{sep} is greater than the time it takes to transduce a noise phonon to an optical photon. Here we have defined t_{sep} to always be greater than this value.

Second, it may happen that both clicks result from thermal emission from either node, one photon in each time bin. There are four such contributions. For the

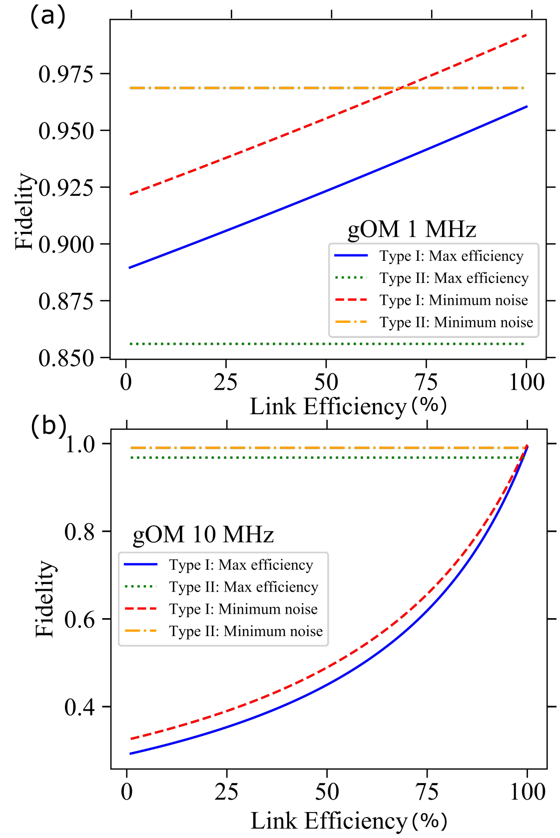

FIG. 9. Entanglement readout fidelity for Type-I and Type-II versus link efficiency for (a)$g_{OM} = 1$ MHz and (b) $g_{OM} = 10$ MHz at $T = 50$ mK. Red curves: Type-I, minimize noise, Blue curves: Type-I, maximize efficiency Gold curves: Type-II, minimize noise, Green curves: Type-I, maximize efficiency.

TABLE II. Example results for FBAR transducers (for $n_{cav} = 625$ mil or $g_{OM} = 10$ MHz and $\Delta = \omega_s$ at 50 mK).

Name	Symbol	1 Ring, Max Eff.	1 Ring, Min Noise	2 Rings, Max Eff.	2 Rings, Min Noise
Motional capacitance	C_m	0.860 fF	0.860 fF	0.860 fF	0.860 fF
Motional inductance	L_m	2.729 μH	2.729 μH	2.729 μH	2.729 μH
Motional resistance	R_m	44.588 Ω	44.588 Ω	44.588 Ω	44.588 Ω
Lorentzian upper sideband	$\mathscr{L}_+^2$	1	1	1	1
Lorentzian lower sideband	$\mathscr{L}_-^2$	$1.303E-4$	$1.303E-4$	$1.303E-4$	$1.303E-4$
Upper sideband resistance 1 ring	$R_{OM,+}$	45.732 Ω	45.732 Ω	N/A	N/A
Lower sideband resistance 1 ring	$R_{OM,-}$	$5.959E-3$ Ω	$5.959E-3$ Ω	N/A	N/A
Equivalent OM resistance 2 ring	R_{OM}^{eq}	N/A	N/A	45.656 Ω	45.656 Ω
Upper sideband resistance 2 ring	$R_{OO,+}$	N/A	N/A	22.908 kΩ	22.908 kΩ
Lower sideband resistance 2 ring	$R_{OO,-}$	N/A	N/A	2.985 Ω	2.985 Ω
Optomechanical cooperativity	C_{OM}	1.026	1.026	1.026	1.026
Optical-optical cooperativity	C_{OO}	N/A	N/A	513.778	513.778
Total optomechanical loading	R_{EM}^{opt}	90.314 Ω	90.314 Ω	90.229 Ω	90.229 Ω
Matching capacitance	C_T	522.346 fF	0 fF	522.680 fF	0 fF
Matching inductance	L	3.246 nH	3.241 nH	3.246 nH	3.239 nH
Matching circuit frequency	$\omega_{LC}/2\pi$	3.287 GHz	3.292 GHz	3.287 GHz	3.292 GHz
Matching circuit quality factor	Q_{LC}	1.347	2.558	1.347	2.558
Electromechanical coupling rate	$g_{EM}/2\pi$	56.640 MHz	107.275 MHz	56.627 MHz	107.475 MHz
Electromechanical cooperativity	C_{EM}	2.025	7.304	2.024	7.301
Electromechanical loading	R_{EM}	90.314 Ω	325.686 Ω	90.229 Ω	325.533 Ω
Conversion efficiency (standard)	η	42.197 %	28.688 %	42.158 %	28.655 %
Conversion efficiency (alt)	η_{alt}	42.197 %	42.197 %	14.556 %	14.556 %
Conversion bandwidth	$\Delta\omega/2\pi$	10.533 MHz	24.257 MHz	10.522 MHz	24.243 MHz
Raman noise quanta	n_o	$6.598E-5$	$1.829E-5$	$6.591E-5$	$1.827E-5$
Thermal noise quanta	n_{th}	$2.203E-2$	$6.110E-3$	$2.205E-2$	$6.112E-3$

TABLE III. Example results for a single-ring FBAR transducer, $T = 50$ mK, $g_{OM} = 10$ MHz (625×10^6 photons in optical cavity), $\eta_l = 50\%$. Qubit reset time is 1 μs, time-bin separation $t_{sep} = \Delta_t + t_r$ and detector efficiency is 90%.

Name	Symbol	Type I Max Eff	Type I Min Noise	Type II Max Eff	Type II Min Noise
Transduction time	Δt	125.655 ns	117.304 ns	125.655 ns	117.304 ns
Photon emission rate	r_o	2.222 MHz	2.222 MHz	2.222 MHz	2.222 MHz
Photon emission probability	P_1	24.364%	22.947%	24.364%	22.947%
Thermal emission probability	P_{th}	0.613%	0.159%	0.613%	0.159%
Photon generation rate	n_r or n_r'	375.252 kHz	359.542 kHz	187.626 kHz	179.771 kHz
Entanglement rate	τ_{ent}	168.863 kHz	161.794 kHz	37.994 kHz	36.403 kHz
Fidelity	F	90.678%	86.516%	92.819%	97.898%

infidelity expression, we have

$$\begin{aligned} P_{in} = 2[&P_{A,E}(1-P_{B,L})P_{th}(1-P_{th})+ \\ &P_{A,L}(1-P_{B,E})P_{th}(1-P_{th})+ \\ &P_{B,E}(1-P_{A,L})P_{th}(1-P_{th})+ \\ &P_{B,L}(1-P_{A,E})P_{th}(1-P_{th})+ \\ &(1-P_{A,E})(1-P_{B,L})P_{th}^2+ \\ &(1-P_{A,L})(1-P_{B,E})P_{th}^2]\eta_l^2 \\ &= (8P_{01}P_{th}(1-P_{th})+4P_{00}P_{th}^2)\eta_l^2 \end{aligned} \quad (68)$$

where the first four terms come from signal/noise false positive events, and the final four terms come from noise/noise false positive events. So the fidelity expression takes the form

$$F = \frac{2P_1^2(1-P_{th})^2}{8P_{01}P_{th}(1-P_{th})+4P_{00}P_{th}^2+2P_1^2(1-P_{th})^2}, \quad (69)$$

where the η_l^2 terms cancel out, rendering the Type-II fidelity independent of link loss (see Figure 10).

For the Type-II infidelity, do we also need to include terms corresponding to thermal photon emission *in addition to* the emission of two signal photons, e.g. a three-photon emission event, where one of the emitted photons is lost before reaching the photodetectors? Fortunately, the answer is no. If we have a situation where the two-click condition is satisfied by one signal photon each in the Early and Late time bins, and we have successfully generated the distributed superconducting qubit Bell pair (Equation 67), the presence of an additional

TABLE IV. Example results for a double-ring FBAR transducer, $T = 50$ mK, $g_{OM} = 10$ MHz (625×10^6 photons in optical cavity), $\eta_l = 50\%$. Qubit reset time is 1 μs, time-bin separation $t_{sep} = \Delta_t + t_r$ and detector efficiency is 90%.

Name	Symbol	Type I Max Eff	Type I Min Noise	Type II Max Eff	Type II Min Noise
Transduction time	Δt_{2MRR}	126.248 ns	117.893 ns	126.248 ns	117.893 ns
Photon emission rate	r_o	2.222 MHz	2.222 MHz	2.222 MHz	2.222 MHz
Photon emission probability	P_1	24.463%	23.048%	24.463%	23.048%
Thermal emission probability	P_{th}	0.617%	0.160%	0.617%	0.160%
Photon generation rate	n_r or n_r'	376.327 kHz	360.683 kHz	188.163 kHz	180.341 kHz
Entanglement rate	τ_{ent}	169.347 kHz	162.307 kHz	38.103 kHz	36.519 kHz
Fidelity	F	90.640%	86.452%	92.817%	97.899%

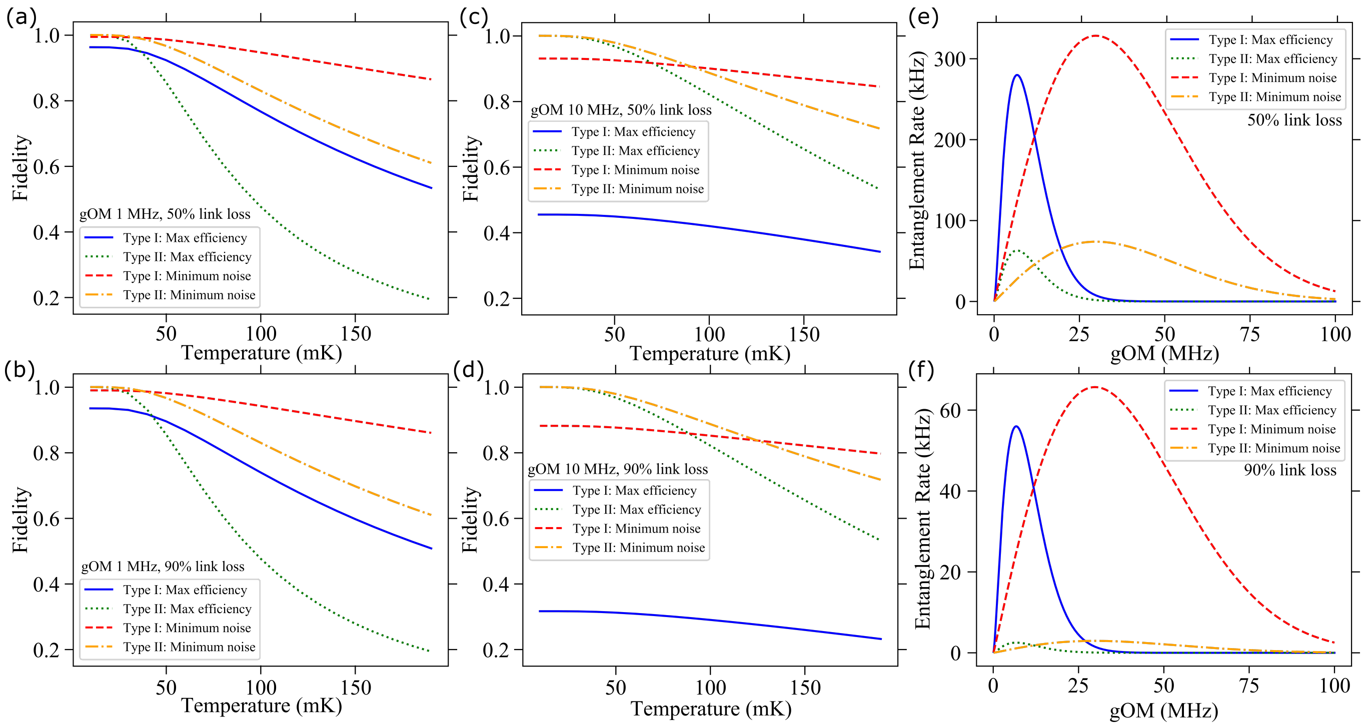

FIG. 10. Type I and Type-II Entanglement fidelity and rate for maximum-efficiency and minimum-noise matching networks, versus temperature, for (a)$g_{OM} = 1$ MHz and $\eta_l = 0.5$, (b)$g_{OM} = 1$ MHz and $\eta_l = 0.1$, (c) $g_{OM} = 10$ MHz and $\eta_l = 0.5$ and (d) $g_{OM} = 10$ MHz and $\eta_l = 0.1$. The entanglement fidelity degrades significantly for the Type-I protocol at higher pump powers (higher g_{OM}), though using a noise-minimizing matching circuit mitigates this effect somewhat. At high temperatures, the fidelity is the worst for the efficiency-maximizing devices, regardless of whether a Type-I or Type-II protocol is used. At low temperatures, the optimal configuration depends on g_{OM}. For a realistic link efficiency of $\eta_l = 0.1$ (b,d), the Type-II protocol with a noise-minimizing matching circuit results in the highest entanglement fidelity at < 50 mK. Plots (e,f) Show the entanglement generation rate versus g_{OM} for (e) $\eta_l = 0.5$ link loss and (f)$\eta_l = 0.1$. As anticipated, Type-II protocols achieve lower entanglement rates than Type-I protocols.

thermal phonon within the transducer will not affect the distributed Bell state. The emissive nature of the direct transduction protocol protects us from this potential source of readout infidelity, assuming that the superconducting qubit is protected by the spurious phonon excitation via a tunable coupling element [66] placed between the transducer and the superconducting qubit that protects the qubit from spurious microwave photon absorption. This protection is not necessarily present for a blue-detuned protocol, as discussed in Appendix E.

The single-photon generation rate for Type-II protocols is, assuming Δt and t_r are the same for both nodes, the same as for Type-I protocols (Equation 59). If we use time-bin encoding, the overall entanglement generation rate is lowered by the time-bin separation t_{sep}, because we need two photon emission events to create our desired Bell state: one each in the Early and Late time bins. The total time it takes to get the two desired emission events is

$$T_{2phot} = 1/(n_r') = \frac{1}{n_r} + t_{sep} - (\Delta_t + t_r) + \frac{1}{n_r} \quad (70)$$

Where n_r' is the modified photon emission rate. If we set

$t_{sep} = \Delta_t + t_r$, we get

$$n_r' = {}^{n_r}/_2 \tag{71}$$

and the expression for the entanglement generation rate is

$$\tau_{ent} = n_r' \eta_l^2 \eta_{det}^2 \tag{72}$$

where the link and detection efficiencies are squares to account for the fact that we need two photon detection events for the protocol to succeed.

C. Entanglement Generation Results

For an FBAR transducer with the parameters summarized in Tables I, II, results are plotted in Figures 6 —10 and summarized in Table III. Note that all results shown are for single-ring devices, with the understanding that results will be similar for two-ring devices.

To ascertain a numerical estimate for the fidelity of the entanglement heralding process for the FBAR transducer, we need to obtain values for P_1, P_{th}, and the associated photon generation rates. For the device parameters listed in Table I, and assuming it takes 1 μs to reset the superconducting qubits between each attempt, we get the values shown in Table III for a single-ring device and Table IV for a double-ring device.

For an FBAR transducer operating at $T = 50$ mK and $g_{OM} = 10$ MHz, the Type-I protocol has a higher entanglement generation rate: 169 kHz for an efficiency-maximizing circuit and 162 kHz for a noise-minimizing circuit, and a fidelity of $\sim 90\%$. For a Type-II protocol, we get entanglement generation rates of about 37 kHz. For both protocols, the fidelity is sensitive to which matching circuit is used, but to different effects. For Type-I, a fidelity of $\sim 90\%$ is achieved for efficiency maximization, and $\sim 86\%$ for noise minimization. The decrease in fidelity for noise minimization can be attributed to the decrease in signal photons relative to false detection events at the high pump power corresponding to $g_{OM} = 10$ MHz. For Type-II, a fidelity of $\sim 93\%$ is achieved for efficiency maximization, and $\sim 98\%$ for noise minimization. Note that the entanglement generation rate is lower for noise-minimizing circuits, despite the fact that the transduction time is faster, due to the slightly lower photon emission probability.

Zeuthen *et al.* [28] found that, for low added noise $n_{th} << 1$ in their transducer, the two-photon protocol is less sensitive to added noise than the one-photon protocol. For the time-bin qubit-based Type-II protocol explored here, the many contributions to infidelity from the presence of thermal excitations make the protocol more sensitive to added noise. As such, the effective implementation of noise-minimizing matching circuits, with low parasitic capacitance, is paramount to high fidelity operation.

In Fig. 6 we plot the fidelity of a Type-I protocol versus the device temperature and optical cavity photon number. The photon numbers plotted correspond to a range $g_{OM} \in [1 \text{ MHz}, 10 \text{ MHz}]$. The top row of the figure shows the fidelity for transducers with efficiency-maximizing circuits, whereas the bottom row has noise-minimizing circuits. Overall, using a noise-minimizing matching circuit maximizes fidelity. The fidelity difference between the two options is more pronounced for lower η_l values. The true value of the noise-minimizing circuits becomes clear at higher temperatures. For example, with $\eta_l = 50\%$, at 150 mK the entanglement fidelity is $> 90\%$ with a noise-minimizing circuit, but is only $60 - 70\%$ for an efficiency-maximizing circuit.

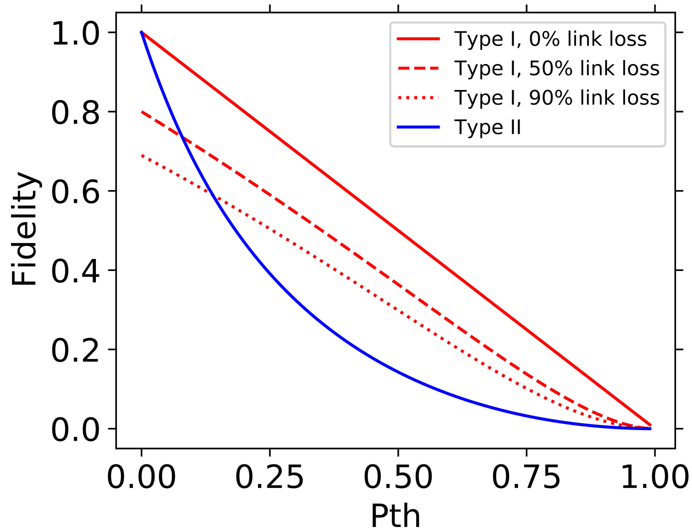

FIG. 11. A comparison of the dependence of Type-I and Type-II readout fidelity on P_{th}. While the Type-II fidelity does not depend on η_l, it falls off more rapidly with increasing P_{th}.

In Figure 10 we plot the fidelity of Type-I and Type-II protocols vs. temperature for efficiency-maximizing and noise-minimizing matching circuits. These are plotted for different g_{OM} values and link efficiencies. For realistic link losses of 90%, we see that Type-II protocols result in higher readout fidelities at higher pump powers, but the Type-II fidelity falls off more steeply with increasing temperature, as these are more sensitive to thermal noise. For a lower g_{OM} in panel (b), the Type-I protocol for a device with a noise-minimizing matching circuit becomes the highest-fidelity option for temperatures of 50 mK and above.

To better understand the relative dependence of the Type-I and Type-II protocols' fidelity on thermal noise, we write out simplified expressions for each protocol's dependence on P_{th}:

$$F_{TypeI} \sim \frac{2(1-P_{th})^2}{(1-P_{th})^2(3-\eta_l) + P_{th}(1-P_{th})(3-\eta_l) + P_{th}^2(1-\eta_l)} \xrightarrow[P_{th}\to 0]{} \frac{2}{3-\eta_l}$$

$$F_{TypeII} \sim \frac{-(1-P_{th})^2}{P_{th}^2 - 2P_{th} - 1} \xrightarrow[P_{th}\to 0]{} 1 \tag{73}$$

These expressions are plotted versus P_{th} in Figure 11, showing how the Type-II readout fidelity falls off steeply with increasing P_{th}. This sensitive dependence on noise further motivates the implementation of noise-minimizing impedance matching networks for the FBAR transducer.

Next, we compare the entanglement generation rate between the two protocols. The results show that higher entanglement generation rates are achievable with Type-I protocols, which is to be expected. For Type-I, using a noise-minimizing circuit decreases the entanglement generation rate by $\sim 5\%$ while achieving about the same readout fidelity. As such, the use of efficiency-maximizing circuits will be preferable, since they will achieve a higher entanglement rate at about the same fidelity and will be easier to fabricate. For the Type-II protocol, doing the same decreases the entanglement generation rate by $\sim 5\%$, while boosting fidelity from 92% to 97%; given the relatively small decrease in entanglement rate, the boost in fidelity justifies the prioritization of noise-minimizing matching circuits, despite the inevitable difficulties in their fabrication.

IV. DISCUSSION AND OUTLOOK

As summarized in Table III, for superconducting qubits networked using impedance-matched FBAR transducers, in a realistic operation regime, we show that entanglement can be achieved at rates of up to 380 kHz and fidelities of $92-98\%$, at a temperature of 50 mK, depending on the matching circuit and the protocol in use. If the superconducting qubits have coherence times of 100 μs, or equivalently, decoherence rates of 10 kHz, we can in principle achieve entanglement at a rate exceeding the decoherence rate of the qubits. With ever-increasing qubit coherence times [67], it will only become easier to reach this performance threshold. This work only explored impedance matching circuits for one set of physical parameters for the FBAR transducer. In practice, the transducer's internal properties, such as its constituent materials, their geometry, and the external optical coupling rate κ_{ext} can be modified to further improve performance tailored for a specific application.

Unlike OMC-based optomechanical transducers that exhibit single-photon optomechanical coupling rates of $10-100$ kHz or more, FBAR transducers will have values of < 1 kHz. While the lower coupling rate can be viewed as a disadvantage, our results show that it can be beneficial. The comparatively low optomechanical loading R_{EM}^{opt} for the FBAR transducers at a given optical pump power requires larger matching capacitances and lower matching inductances, as compared to OMC-based transducers [27], which makes the design and fabrication of the matching networks more feasible. This allows the transducer's piezo-mechanical components to have a higher static capacitance, enabling realistic fabrication targets, and allows for more accurate matching circuit designs factoring in non-idealities such as non-zero resistance R_L and parasitic capacitances and inductances.

Going forward, our model can be improved by treating the optomechanical coupling rate and temperature of the device as dependent variables, instead of independent variables. To do this, a mathematical relationship between the optical pump power to the device and the device's temperature must be established. The relationship will depend on the properties of the transducer's optical cavity, the facet loss and scattering at the optical fiber-to-chip interface, the degree of thermal anchoring of the device packaging to the cryostat, the cryostat's cooling power, and more. Defining the relationship between g_{OM} and device temperature for FBAR transducers is an active area of experimental and theoretical exploration. Results obtained from simulations [68] and measurements in the near term will be used to clarify this relationship.

ACKNOWLEDGMENTS

We wish to thank Hao Tian, Alaina Attanasio, and Sunil Bhave of the OxideMEMS laboratory at Purdue University for providing our team with FBAR transducers, helping us learn about how they work, and for a fruitful collaboration.

V. AUTHOR CONTRIBUTIONS

E.S., S.S., M.S., D.C. and T.W. designed transducers and matching networks and performed simulations to verify design parameters. E.S., Z.S., D.H. and D.C. designed the entanglement heralding protocols. E.S., E.A., J.S., S.S. and S.M. performed theoretical calculations. E.S. and M.L. directed and supervised the project. All authors contributed to writing the manuscript.

VI. CONFLICTS OF INTEREST

The authors declare no conflicts of interest.

VII. FUNDING ACKNOWLEDGMENTS

E.S. gratefully acknowledges funding from the Air Force Office of Scientific Research's Protostar LRIR program, under award 25RICOR003.

Appendix A: Adding transducer static resistance into Extended BVD model

As mentioned in the main text, the mBVD model captures the behavior of piezo-mechanical devices more accurately than the standard BVD model. As such, here, we re-derive relevant expressions for a transducer's equivalent circuit with a nonzero static resistance R_0 within the piezo-mechanical sub-circuit.

The electrical LC impedance becomes

$$Z_e(\omega) = -i\omega L + Z_{tx} + R_L + \frac{1}{-i\omega(C_0 + C_T)} \rightarrow$$
$$Z'_e(\omega) = -i\omega L + \left(\frac{1}{Z_{tx} + R_L} + \frac{1}{R_0}\right)^{-1} + \frac{1}{-i\omega(C_0 + C_T)} \tag{A1}$$

This new impedance leads to a modified quality factor of the LC transformer:

$$Q'_{LC} = \frac{1}{\left[(Z_{tx} + R_L)^{-1} + R_0^{-1}\right]^{-1}} \sqrt{\frac{L}{C_T + C_0}} \tag{A2}$$

with an associated electromechanical loading factor

$$R'_{EM} = Q'^2_{LC} \left[(Z_{tx} + R_L)^{-1} + R_0^{-1}\right]^{-1}. \tag{A3}$$

Matching circuit expressions, including the matching capacitance

$$C'_T = \frac{C_m}{2}\left[\sqrt{1 + \frac{4}{R^{opt}_{EM}\omega_s^2 C_m^2 \left(\frac{(Z_{tx}+R_L)R_0}{Z_{tx}+R_L+R_0}\right)}} - 1\right] - C_0 \tag{A4}$$

angular frequency

$$\omega'_m = \sqrt{\frac{1}{L_m}\left(\frac{1}{C_m} + \frac{1}{C'_T + C_0}\right)} \tag{A5}$$

and inductance

$$L' = \frac{1}{\omega'_m}\sqrt{R^{opt}_{EM}\left(\frac{(Z_{tx} + R_L)R_0}{Z_{tx} + R_L + R_0}\right)}. \tag{A6}$$

Appendix B: $R_L \neq 0$ from dielectric loss

In the main text, as in previous work, we assumed that for a superconducting circuit, the matching circuit is lossless, leading to a resistance $R_L = 0\ \Omega$ in the equivalent circuit. For real devices, there will be nonzero loss.

Here we consider a matching network that is fabricated on a substrate with a nonzero loss tangent $\tan(\delta)$.

The matching capacitor C_T will have a loss term associated with dielectric loss, referred to as an equivalent series resistance R_{CT}. For a dielectric layer with loss tangent $\tan(\delta)$, a capacitor with ideal capacitance C_T at angular frequency ω_{LC} has [69]

$$R_{CT} = \frac{\tan(\delta)}{\omega_{LC} C_T} \tag{B1}$$

Similarly, the matching inductor L has an equivalent resistance

$$R_{ind} = \tan(\delta)\omega_{LC} L. \tag{B2}$$

The quality factor of the matching network for $R_L, R_0 \neq 0$ is shown in Equation A2, where we set $R_L = R_{CT} + R_{ind}$.

If the matching network is comprised of an Al thin film deposited on thermal SiO_2 with a loss tangent of approximately 3×10^{-4} [70], we have

$$R_L = tan(\delta)\left(\frac{1}{\omega_{LC} C_T} + \omega_{LC} L\right) = 47.925\ \text{m}\Omega. \tag{B3}$$

Appendix C: Matching inductor parasitic capacitance

The formalism developed the main text, like previous work, ignores stray capacitances associated with the

TABLE V. Difference in matching circuit (maximize efficiency) and transducer (single ring) values for $R_L = 0\ \Omega$ vs. $R_L \neq 0\ \Omega$.

Symbol	$R_L = 0\ \Omega$	$R_L = 47.925\ \text{m}\Omega$
C_m	0.860 fF	0.860 fF
L_m	2.729 μH	2.729 μH
R_m	44.588 Ω	44.588 Ω
$\mathscr{L}_+^2$	1	1
$\mathscr{L}_-^2$	$1.303E-4$	$1.303E-4$
$R_{OM,+}$	45.732 Ω	45.732 Ω
$R_{OM,-}$	$5.959E-3\ \Omega$	$5.959E-3\ \Omega$
C_{OM}	1.026	1.026
R_{EM}^{opt}	90.314 Ω	90.314 Ω
C_T	522.346 fF	522.002 fF
L	3.246 nH	3.247 nH
$\omega_{LC}/2\pi$	3.287 GHz	3.287 GHz
Q_{LC}	1.347	1.347
$g_{EM}/2\pi$	56.640 MHz	56.654 MHz
C_{EM}	2.025	2.026
R_{EM}	90.314 Ω	90.314 Ω
η	42.197 %	42.197 %
η_{alt}	42.197 %	42.197 %
$\Delta\omega/2\pi$	10.533 MHz	10.533 MHz
n_o	$6.598E-5$	$6.598E-5$
n_{th}	$2.203E-2$	$2.203E-2$

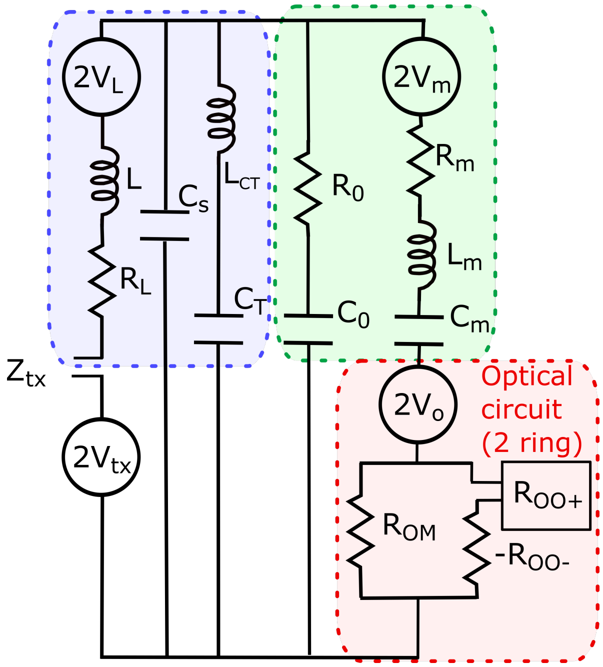

FIG. 12. A modified equivalent circuit for a transducer with parasitic terms incorporated into the matching network.

matching inductor L in the equivalent circuit model. This is despite the large matching inductances and small matching capacitances often required for OMC-based transducers [27], which may require large spiral inductors that have large stray, or parasitic, capacitances. The stray inductance of the matching capacitor should also be considered. In this section we examine the stray capacitances and inductances of the matching elements and their effect on impedance-matched transducer design.

We start with the matching inductor. There will be two parasitic capacitive terms: the inductor's self-capacitance, and its capacitance to ground. The first arises from the inherent capacitance that exists within the inductor, including capacitances between adjacent wires within a meandering or spiral structure, and the second arises from an unwanted capacitance between the inductor metal and the nearby ground-plane metal layer. For superconducting spiral inductors, previous studies have found inductors fabricated on Silicon with inductances of $3-7$ nH to have self-capacitances of about 5 fF [71]. Additional capacitance to the ground plane must also be considered, which may add an additional $5-10$ fF or more [72, 73]. For a nanowire inductor made of a high-kinetic inductance material such as niobium nitride (NbN) [61], a 40 nm-wide nanowire has an inductance of 2.05 mH/m and a capacitance of 44 pF/m. A target inductance of 3.247 nH would require a length of 1.584 μm, corresponding to a capacitance of 70 aF and a self-resonance at 2 THz.

These considerations motivate a modification of the matching network design formalism to account for stray capacitances. The inductor's parasitic capacitance $C_p = C_s + C_g$, where C_s is its self capacitance and C_g is its capacitance to ground. C_p will be added in parallel to the intentionally designed matching capacitor C_T, leading to a modified equivalent matching capacitance C'_T:

$$C'_T = C_T + C_p. \tag{C1}$$

Next we consider the stray inductance L_{CT} of the matching capacitor. This parasitic term will add in series with the existing inductance L, for a modified equivalent matching inductance L':

$$L' = L + L_{CT}. \tag{C2}$$

A modified equivalent circuit incorporating the parasitic terms into the matching network is shown in Fig. 11. To design a matching circuit that incorporates the parasitic terms, we follow the process outlined in the main text, using Equations 33-36. The values we obtain from those expressions are C'_T and L'. Next, we use simulations or numerical estimates to obtain values for the parasitic terms C_p and L_{CT}. Finally, we modify the matching network components L, C_T as follows:

$$C_T = C'_T - C_p \quad ; \quad L = L' - L_{CT}. \tag{C3}$$

Clearly, the modified components will have slightly different parasitic values than originally estimated. If desired, this process can be iterated to obtain more and more accuracy.

Appendix D: Bell-State Analysis for Time-Bin Photons

In the main text, we implement a Type-II entanglement heralding protocol based on time-bin encoding of photon qubits. The use of the time-bin basis leads to a question of how Bell state analysis will be performed.

For time-bin photons, we have two options. We could use a balanced Bell state analyzer, within which the two path lengths are equal, or an unbalanced Bell state analyzer, in which the path length difference between the two arms is equal to the time bin separation. Let's explore the benefits and drawbacks of these two options.

Time bin qubits can be measured using a simple (balanced) Bell state analyzer with a non-polarizing 50:50 beamsplitter and two SNSPDs. With sufficient temporal resolution, this setup can be used to project a two-photon state onto $|\Psi^-\rangle$ or $|\Psi^+\rangle$. Here, the different Bell state projections correspond to different temporal detection patterns[74]. Specifically, if one detector registers a photon in the Early bin and the other detector registers a photon in the Late bin, the photons are projected into $|\Psi^-\rangle$. The $|\Psi^+\rangle$ state is projected when the same detector registers both Early and Late photons. The photonic Bell states, with early (E) and late (L) photons emerging from nodes A and B, take the form

$$|\Psi^-_{phot-A,B}\rangle = \frac{1}{\sqrt{2}}(|1_E 0_L\rangle_A |0_E 1_L\rangle_B - |0_E 1_L\rangle_A |1_E 0_L\rangle_B)$$
$$|\Psi^+_{phot-A,B}\rangle = \frac{1}{\sqrt{2}}(|1_E 0_L\rangle_A |0_E 1_L\rangle_B + |0_E 1_L\rangle_A |1_E 0_L\rangle_B) \quad \text{(D1)}$$

If we assume that the single photon detectors employed within the BSA can resolve the arrival time of photons with a given time-bin separation, we can proceed to use a balanced interferometer for Bell state measurements. Of course, this requires the dead time of the detector to be shorter than the time bin separation. For our chosen time-bin separation of 500 ns, this requirement can be satisfied, as commercial SNSPDs have dead times falling in the $10 - 100$ ns range. Assuming both $|\Psi^-\rangle$ and $|\Psi^+\rangle$ can be resolved, the BSA has a maximum efficiency of 50%.

Alternatively, we may use an unbalanced BSA, or a time-domain interferometer (TDI). One arm of the TDI has a delay line that applies a time delay equal to the time-bin separation, Δt, allowing for the erasure of which-time-bin information. Coincidence events occur when Early photons propagate through the long arm and Late photons propagate through the short arm. This will occur 50% of the time for early-late input pairs. The other 50% of the time, the Late photons will travel through the long arm, and vice versa, doubling the time delay between Early and Late. If we throw away non-coincident detection events, we are only able to distinguish the $|\Psi^-\rangle$ state.

Another drawback of this measurement method is the need to actively stabilize the interferometer's long delay line. Fiber-based delay lines are susceptible to perturbations due to environmental vibrations and temperature fluctuations. The time delay must be stabilized using active components such as fiber piezo-stretchers controlled by feedback loops within periodic calibration measurements. This benefit of this additional overhead carries the advantage of eliminating strict requirements on the reset time of the single photon detectors and simplifying post-detection analysis.

Appendix E: Blue-Detuned Transducer Operation

For completeness, here we consider entanglement heralding protocols that utilize spontaneous parametric down conversion (SPDC) in a blue-detuned transducer to generate entangled microwave-telecom photon pairs. This scenario is briefly explored using a formalism similar to out own in references [12, 59] but not in [46]. Blue-detuned operation with a Type-II protocol using time-bin photons, but not with a Type-I protocol, is explored in depth in reference [30].

For a Type-I protocol utilizing SPDC seeded by a blue-detuned transducer pump, each of two identical nodes produces entangled microwave-optical photon pairs. The microwave photon is converted to a superconducting qubit excitation via stimulated Raman absorption, while the optical photon is emitted by the transducer toward the BSA. The detection of an optical photon in the BSA (a single-click event) heralds the production of a single microwave photon. For a qubit initialized in its ground state, detection of an optical photon corresponds to the qubit being in its excited state. In a simplified picture, the qubit-cavity system begins in the state $|1_m\rangle |g\rangle$, where m denotes the microwave mode. Absorption of the photon via a Jaynes-Cummings interaction evolves the system to the state $|0_m\rangle |e\rangle$.

A Type-I heralding protocol based on this process pumps two copies of a system and, as detailed above, erases which-path information on a beamsplitter to herald a distributed microwave photon Bell pair. A successful attempt produces the target photonic Bell state in Equation 54, which projects the remote superconducting qubits into the distributed Bell state

$$|\Psi\rangle = \sqrt{P_{01}}\,|g_A e_B\rangle + \sqrt{P_{10}}\,|e_A g_B\rangle \quad \text{(E1)}$$

As discussed in [12, 29], this protocol is susceptible to additional source of readout infidelity. SPDC-based protocols allow for multi-photon generation events [59], where instead of a microwave optical pair $|1_m\rangle |1_o\rangle$, the process generates $|N_m\rangle |N_o\rangle$ pairs, where $N > 1$. In the absence of number-resolving detectors, an N-photon generation event may satisfy the one-click condition of the protocol, generating a false positive event. Furthermore, the presence of multi-photon Fock states in the transducer's microwave cavity may lead to multi-photon absorption events in the superconducting qubit, and other deleterious behaviors, such as qubit dephasing and spurious excitations due to residual population of the microwave cavity. Following [59], we list the infidelity contributions from multi-photon excitation events below.

Probability that node A(B) emits a multi-photon state and node B(A) emits zero photons, and the emitted photon reaches the BSA:

$$P_{multi,0} = P_0(1 - P_0 - P_1)\eta_l \quad \text{(E2)}$$

There are two such contributions. There are also two contributions from single photon emission from node A(B), and multi-photon emission from node B(A), where one photon packet is lost and the other reaches the BSA:

$$P_{multi,1} = P_1(1 - P_0 - P_1)\eta_l(1 - \eta_l) \quad \text{(E3)}$$

Finally, it may happen that both nodes undergo multi-photon emission, and one of the emitted photon packets is lost before reaching the BSA:

$$P_{multi,multi} = (1 - P_0 - P_1)^2\eta_l(1 - \eta_l). \quad \text{(E4)}$$

Putting it together, we get the infidelity expression:

$$\begin{aligned} P_{in} = P_1^2\eta_l(1 - \eta_l) + \\ 2P_1(1 - P_1 - P_0)\eta_l + \\ 2P_1(1 - P_0 - P_1)\eta_l(1 - \eta_l) + \\ (1 - P_0 - P_1)^2\eta_l(1 - \eta_l). \end{aligned} \quad \text{(E5)}$$

It's important to note that multi-photon events impact the *entanglement* fidelity of the transducer, in addition to the readout fidelity of the heralding protocol. This caveat is discussed further below. Going beyond this analysis to include additional contributions to infidelity from thermal noise present in the transducer is a nontrivial task, and is explored in reference [30].

Putting aside multi-photon generation events, thermal quanta lead to additional false positive detection events, as well as additional problematic phenomena. First, the presence of thermal populations in the transducer's modes decreases the achievable entanglement fidelity within the device: thermal quanta reduce the degree of squeezing in the transducer, thereby reducing the purity of the entangled microwave-optical photon pair [30]. Second, since the superconducting qubit is operating in an absorptive manner, it will absorb microwave photons emitted by the transducer, whether those photons were generated via SPDC or via thermal population of the transducer's acoustic mode. Therefore, regardless of the optical photon click pattern observed, the superconducting qubits within each node may be in a state other than what was supposedly heralded.

To make matters worse, when we are operating the superconducting qubit as an absorber, we must properly shape the microwave photon emitted by the transducer to facilitate absorption [75], adding additional complexity to the protocol. Efficiently capturing or detecting an arbitrarily shaped microwave photon with a superconducting qubit remains an outstanding challenge. Given these considerations, in addition to the order of magnitude lower readout fidelity obtained in previous studies [12, 59], we focus on the direct transduction protocol in this work.

[1] N. J. Lambert, A. Rueda, F. Sedlmeir, and H. G. L. Schwefel, Advanced Quantum Technologies **3**, 10.1002/qute.201900077 (2020).

[2] N. Lauk, N. Sinclair, S. Barzanjeh, J. P. Covey, M. Saffman, M. Spiropulu, and C. Simon, Quantum Science and Technology **5**, 020501 (2020).

[3] X. Han, W. Fu, C.-L. Zou, L. Jiang, and H. X. Tang, Optica **8**, 1050 (2021).

[4] S. Wehner, D. Elkouss, and R. Hanson, Science **362**, 10.1126/science.aam9288 (2018).

[5] G. Guccione, T. Darras, H. L. Jeannic, V. B. Verma, S. W. Nam, A. Cavaillès, and J. Laurat, Science Advances **6**, 10.1126/sciadv.aba4508 (2020).

[6] J. Ang, G. Carini, Y. Chen, I. Chuang, M. Demarco, S. Economou, A. Eickbusch, A. Faraon, K.-M. Fu, S. Girvin, M. Hatridge, A. Houck, P. Hilaire, K. Krsulich, A. Li, C. Liu, Y. Liu, M. Martonosi, D. McKay, J. Misewich, M. Ritter, R. Schoelkopf, S. Stein, S. Sussman, H. Tang, W. Tang, T. Tomesh, N. Tubman, C. Wang, N. Wiebe, Y. Yao, D. Yost, and Y. Zhou, ACM Transactions on Quantum Computing **5**, 1 (2024).

[7] A. S. Cacciapuoti, M. Caleffi, F. Tafuri, F. S. Cataliotti, S. Gherardini, and G. Bianchi, IEEE Network **34**, 137 (2020).

[8] J. Larson, P. Bradley, S. Wartenberg, and R. Ruby, in *2000 IEEE Ultrasonics Symposium. Proceedings. An International Symposium (Cat. No.00CH37121)* (IEEE, 2000) pp. 863–868 vol.1.

[9] L.-M. Duan, M. D. Lukin, J. I. Cirac, and P. Zoller, Nature **414**, 413 (2001).

[10] S. D. Barrett and P. Kok, Physical Review A **71**, 060310 (2005).

[11] M. M. Wolf, D. Pérez-García, and G. Giedke, Physical Review Letters **98**, 130501 (2007).

[12] S. Krastanov, H. Raniwala, J. Holzgrafe, K. Jacobs, M. Lončar, M. J. Reagor, and D. R. Englund, Physical Review Letters **127**, 40503 (2021).

[13] D. L. Moehring, P. Maunz, S. Olmschenk, K. C. Younge, D. N. Matsukevich, L.-M. Duan, and C. Monroe, Nature **449**, 68 (2007).

[14] P. Maunz, S. Olmschenk, D. Hayes, D. N. Matsukevich, L.-M. Duan, and C. Monroe, Physical Review Letters **102**, 250502 (2009).

[15] S. Olmschenk, D. N. Matsukevich, P. Maunz, D. Hayes, L.-M. Duan, and C. Monroe, Science **323**, 486 (2009).

[16] D. Hucul, I. V. Inlek, G. Vittorini, C. Crocker, S. Debnath, S. M. Clark, and C. Monroe, Nature Physics **11**, 37 (2015).

[17] V. Krutyanskiy, M. Galli, V. Krcmarsky, S. Baier, D. Fioretto, Y. Pu, A. Mazloom, P. Sekatski, M. Canteri, M. Teller, J. Schupp, J. Bate, M. Meraner, N. Sangouard, B. Lanyon, and T. Northup, Physical Review Letters **130**, 050803 (2023).

[18] B. Hensen, H. Bernien, A. E. Dréau, A. Reiserer, N. Kalb, M. S. Blok, J. Ruitenberg, R. F. L. Vermeulen, R. N. Schouten, C. Abellán, W. Amaya, V. Pruneri, M. W. Mitchell, M. Markham, D. J. Twitchen, D. Elkouss, S. Wehner, T. H. Taminiau, and R. Hanson, Nature **526**, 682 (2015).

[19] M. Pompili, S. L. N. Hermans, S. Baier, H. K. C. Beukers, P. C. Humphreys, R. N. Schouten, R. F. L. Vermeulen, M. J. Tiggelman, L. dos Santos Martins, B. Dirkse, S. Wehner, and R. Hanson, Science **372**, 259 (2021).

[20] A. J. Stolk, K. L. van der Enden, M.-C. Slater, I. te Raa-Derckx, P. Botma, J. van Rantwijk, B. Biemond, R. A. J. Hagen, R. W. Herfst, W. D. Koek, A. J. H. Meskers, R. Vollmer, E. J. van Zwet, M. Markham, A. M. Edmonds, J. F. Geus, F. Elsen, B. Jungbluth, C. Haefner, C. Tresp, J. Stuhler, S. Ritter, and R. Hanson, arXiv (2024).

[21] A. Narla, S. Shankar, M. Hatridge, Z. Leghtas, K. Sliwa, E. Zalys-Geller, S. Mundhada, W. Pfaff, L. Frunzio, R. Schoelkopf, and M. Devoret, Physical Review X **6**, 031036 (2016).

[22] P. Kurpiers, P. Magnard, T. Walter, B. Royer, M. Pechal, J. Heinsoo, Y. Salathé, A. Akin, S. Storz, J.-C. Besse, S. Gasparinetti, A. Blais, and A. Wallraff, Nature **558**, 264 (2018).

[23] C. Dickel, J. J. Wesdorp, N. K. Langford, S. Peiter, R. Sagastizabal, A. Bruno, B. Criger, F. Motzoi, and L. DiCarlo, Physical Review B **97**, 064508 (2018).

[24] M. Mirhosseini, A. Sipahigil, M. Kalaee, and O. Painter,

Nature **588**, 599 (2020).
[25] T. C. van Thiel, M. J. Weaver, F. Berto, P. Duivestein, M. Lemang, K. L. Schuurman, M. Žemlička, F. Hijazi, A. C. Bernasconi, C. Ferrer, E. Lachman, M. Field, Y. Mohan, F. K. de Vries, C. C. Bultink, J. van Oven, J. Y. Mutus, R. Stockill, and S. Gröblacher, arXiv preprint (2023).
[26] T. Blésin, H. Tian, S. A. Bhave, and T. J. Kippenberg, Physical Review A **104**, 52601 (2021).
[27] M. Wu, E. Zeuthen, K. C. Balram, and K. Srinivasan, Physical Review Applied **13**, 014027 (2020).
[28] E. Zeuthen, A. Schliesser, A. S. Sørensen, and J. M. Taylor, Quantum Science and Technology **5**, 034009 (2020).
[29] C. Zhong, X. Han, H. X. Tang, and L. Jiang, Physical Review A **101**, 032345 (2020).
[30] C. Zhong, Z. Wang, C. Zou, M. Zhang, X. Han, W. Fu, M. Xu, S. Shankar, M. H. Devoret, H. X. Tang, and L. Jiang, Physical Review Letters **124**, 010511 (2020).
[31] L. d'Avossa, M. Caleffi, C. Wang, J. Illiano, S. Zorzetti, and A. S. Cacciapuoti, 2023 IEEE International Conference on Quantum Computing and Engineering (QCE) , 1325 (2023).
[32] S. Meesala, S. Wood, D. Lake, P. Chiappina, C. Zhong, A. D. Beyer, M. D. Shaw, L. Jiang, and O. Painter, Nature Physics **20**, 871 (2024).
[33] M. J. Weaver, P. Duivestein, A. C. Bernasconi, S. Scharmer, M. Lemang, T. C. van Thiel, F. Hijazi, B. Hensen, S. Gröblacher, and R. Stockill, Nature Nanotechnology **19**, 166 (2024).
[34] H. Ren, M. H. Matheny, G. S. MacCabe, J. Luo, H. Pfeifer, M. Mirhosseini, and O. Painter, Nature Communications **11**, 3373 (2020).
[35] F. M. Mayor, S. Malik, A. G. Primo, S. Gyger, W. Jiang, T. P. M. Alegre, and A. H. Safavi-Naeini, arXiv (2024).
[36] S. Sonar, U. Hatipoglu, S. Meesala, D. Lake, H. Ren, and O. Painter, High-efficiency low-noise optomechanical crystal photon-phonon transducers (2024), arXiv:2406.15701 [physics.optics].
[37] H. Tian, J. Liu, B. Dong, J. C. Skehan, M. Zervas, T. J. Kippenberg, and S. A. Bhave, Nature Communications **11**, 3073 (2020).
[38] T. Blésin, W. Kao, A. Siddharth, R. N. Wang, A. Attanasio, H. Tian, S. A. Bhave, and T. J. Kippenberg, Nature Communications **15**, 6096 (2024).
[39] J. Schneeloch, E. Sheridan, A. M. Smith, C. C. Tison, D. L. Campbell, M. D. LaHaye, M. L. Fanto, and P. M. Alsing, arXiv **2312.04673** (2023).
[40] Y. Liu, Y. Cai, Y. Zhang, A. Tovstopyat, S. Liu, and C. Sun, Micromachines **11**, 630 (2020).
[41] Vinita, D. Pareek, S. M. Islam, and J. Singh, Sensors and Actuators A: Physical **378**, 115839 (2024).
[42] H. M. Doeleman, T. Schatteburg, R. Benevides, S. Vollenweider, D. Macri, and Y. Chu, Physical Review Research **5**, 043140 (2023).
[43] H. Tian, J. Liu, A. Attanasio, A. Siddharth, T. Blesin, R. N. Wang, A. Voloshin, G. Lihachev, J. Riemensberger, S. E. Kenning, Y. Tian, T. H. Chang, A. Bancora, V. Snigirev, V. Shadymov, T. J. Kippenberg, and S. Bhave, Piezoelectric actuation for integrated photonics (2024), arXiv:2405.08836 [physics.optics].
[44] Y. Chu, P. Kharel, W. H. Renninger, L. D. Burkhart, L. Frunzio, P. T. Rakich, and R. J. Schoelkopf, Science **358**, 199 (2017).
[45] Y. Chu, P. Kharel, T. Yoon, L. Frunzio, P. T. Rakich, and R. J. Schoelkopf, Nature **563**, 666 (2018).
[46] E. Zeuthen, A. Schliesser, J. M. Taylor, and A. S. Sørensen, Physical Review Applied **10**, 044036 (2018).
[47] I. S. Uzunov, M. D. Terzieva, B. M. Nikolova, and D. G. Gaydazhiev, in *2017 XXVI International Scientific Conference Electronics (ET)* (IEEE, 2017) pp. 1–4.
[48] L. Luo, D. Hayes, T. Manning, D. Matsukevich, P. Maunz, S. Olmschenk, J. Sterk, and C. Monroe, Fortschritte der Physik **57**, 1133 (2009).
[49] R. Stockill, M. Stanley, L. Huthmacher, E. Clarke, M. Hugues, A. Miller, C. Matthiesen, C. L. Gall, and M. Atatüre, Physical Review Letters **119**, 010503 (2017).
[50] M. Aspelmeyer, T. J. Kippenberg, and F. Marquardt, Reviews of Modern Physics **86**, 1391 (2014).
[51] W. Jiang, F. M. Mayor, S. Malik, R. V. Laer, T. P. McKenna, R. N. Patel, J. D. Witmer, and A. H. Safavi-Naeini, Nature Physics **19**, 1423 (2023).
[52] M. D. LaHaye, J. Suh, P. M. Echternach, K. C. Schwab, and M. L. Roukes, Nature **459**, 960 (2009).
[53] N. Ares, F. Schupp, A. Mavalankar, G. Rogers, J. Griffiths, G. Jones, I. Farrer, D. Ritchie, C. Smith, A. Cottet, G. Briggs, and E. Laird, Physical Review Applied **5**, 034011 (2016).
[54] D. M. Pozar, *Microwave engineering; 3rd ed.* (Wiley, Hoboken, NJ, 2005) Chap. 5.
[55] S. Chang, N. Rogacheva, and C. Chou, IEEE Transactions on Ultrasonics, Ferroelectrics, and Frequency Control **42**, 630 (1995).
[56] S. Sridaran and S. A. Bhave, Optics Express **19**, 9020 (2011).
[57] C.-H. Wang, M. Zhang, and L. Jiang, Physical Review Research **4**, L042023 (2022).
[58] M. Zhang, C. Wang, Y. Hu, A. Shams-Ansari, T. Ren, S. Fan, and M. Lončar, Nature Photonics **13**, 36 (2019).
[59] C. Wang, I. Gonin, A. Grassellino, S. Kazakov, A. Romanenko, V. P. Yakovlev, and S. Zorzetti, npj Quantum Information **8**, 149 (2022).
[60] A. Siddharth, A. Attanasio, S. Bianconi, G. Lihachev, J. Zhang, Z. Qiu, A. Bancora, S. Kenning, R. N. Wang, A. S. Voloshin, S. A. Bhave, J. Riemensberger, and T. J. Kippenberg, Optica **11**, 1062 (2024).
[61] D. Niepce, J. Burnett, and J. Bylander, Physical Review Applied **11**, 044014 (2019).
[62] P. Kurpiers, M. Pechal, B. Royer, P. Magnard, T. Walter, J. Heinsoo, Y. Salathé, A. Akin, S. Storz, J.-C. Besse, S. Gasparinetti, A. Blais, and A. Wallraff, Physical Review Applied **12**, 044067 (2019).
[63] J. Ilves, S. Kono, Y. Sunada, S. Yamazaki, M. Kim, K. Koshino, and Y. Nakamura, npj Quantum Information **6**, 34 (2020).
[64] A. Tchebotareva, S. L. Hermans, P. C. Humphreys, D. Voigt, P. J. Harmsma, L. K. Cheng, A. L. Verlaan, N. Dijkhuizen, W. de Jong, A. Dréau, and R. Hanson, Physical Review Letters **123**, 063601 (2019).
[65] E. Bersin, M. Sutula, Y. Q. Huan, A. Suleymanzade, D. R. Assumpcao, Y.-C. Wei, P.-J. Stas, C. M. Knaut, E. N. Knall, C. Langrock, N. Sinclair, R. Murphy, R. Riedinger, M. Yeh, C. Xin, S. Bandyopadhyay, D. D. Sukachev, B. Machielse, D. S. Levonian, M. K. Bhaskar, S. Hamilton, H. Park, M. Lončar, M. M. Fejer, P. B. Dixon, D. R. Englund, and M. D. Lukin, PRX Quantum **5**, 010303 (2024).
[66] D. L. Campbell, A. Kamal, L. Ranzani, M. Senatore, and M. D. LaHaye, Physical Review Applied **19**, 64043

(2023).
[67] C. Wang, X. Li, H. Xu, Z. Li, J. Wang, Z. Yang, Z. Mi, X. Liang, T. Su, C. Yang, G. Wang, W. Wang, Y. Li, M. Chen, C. Li, K. Linghu, J. Han, Y. Zhang, Y. Feng, Y. Song, T. Ma, J. Zhang, R. Wang, P. Zhao, W. Liu, G. Xue, Y. Jin, and H. Yu, npj Quantum Information **8**, 3 (2022).
[68] B. Ivira, R.-Y. Fillit, F. Ndagijimana, P. Benech, G. Parat, and P. Ancey, IEEE Transactions on Ultrasonics, Ferroelectrics and Frequency Control **55**, 139 (2008).
[69] S. M. Riad and I. M. Salama, Electromagnetic fields and waves: Fundamentals of engineering, 1st edition (McGraw-Hill Education, 2020) Chap. ADDENDUM 11D: LOSS TANGENT FOR ENERGY-STORAGE MEDIA (MATERIALS) AND DEVICES, 1st ed.
[70] A. D. O'Connell, M. Ansmann, R. C. Bialczak, M. Hofheinz, N. Katz, E. Lucero, C. McKenney, M. Neeley, H. Wang, E. M. Weig, A. N. Cleland, and J. M. Martinis, Applied Physics Letters **92**, 10.1063/1.2898887 (2008).
[71] M. Peruzzo, A. Trioni, F. Hassani, M. Zemlicka, and J. M. Fink, Physical Review Applied **14**, 044055 (2020).
[72] J. W. Hooker, V. Ramaswamy, R. K. Arora, A. S. Edison, and W. W. Brey, IEEE Transactions on Applied Superconductivity **26**, 1 (2016).
[73] W. W. Xue, B. Davis, F. Pan, J. Stettenheim, T. J. Gilheart, A. J. Rimberg, and Z. Ji, Applied Physics Letters **91**, 10.1063/1.2776888 (2007).
[74] R. Valivarthi, I. Lucio-Martinez, A. Rubenok, P. Chan, F. Marsili, V. B. Verma, M. D. Shaw, J. A. Stern, J. A. Slater, D. Oblak, S. W. Nam, and W. Tittel, Opt. Express **22**, 24497 (2014).
[75] C. Zhong, Physical Review Research **6**, 043196 (2024).